PERGAMON

Journal of Structural Geology 25 (2003) 1691–1711

JOURNAL OF STRUCTURAL GEOLOGY

www.elsevier.com/locate/jsg

The impact of analogue material properties on the geometry, kinematics, and dynamics of convergent sand wedges

Jo Lohrmann*, Nina Kukowski, Jürgen Adam, Onno Oncken

GeoForschungsZentrum Potsdam, Projektbereich 3.1, Telegrafenberg, D-14473Potsdam, Germany

Received 7 July 2001

Abstract

Simulation of geodynamic processes in sandbox experiments requires analogue materials with a deformation behaviour that reproduces the deformation mechanisms of typical crustal rocks. We present data on the frictional strength of different sand types employing static and dynamic shear tests. The sand types analysed are characterised by an elastic/frictional plastic mechanical behaviour with a transient strain-hardening and strain-softening phase prior to transition to stable sliding. This is in conflict with the standard assumption of an ideal cohesionless Coulomb-material with constant frictional properties. The influence of the identified transient material properties on the kinematics, growth mechanisms, and internal deformation patterns of convergent sand wedges results in characteristic wedge segments which vary—depending on material compaction—between wedges with well defined segments (i.e. frontal-deformation zone, frontal-imbrication zone and internal-accumulation zone) with straight slopes and wedges with a continuous convex topographic profile. For most materials, only the frontal part of the wedge is critical during experimental runs. Taper and strength of the wedge segments can be shown to be controlled by the frictional properties of active faults. Wedge segmentation is controlled by a bulk-strength increase toward the rear of the wedge due to fault rotation in mechanically less-favourable orientations and plastic material hardening. The limit between the frontal critical parts of a wedge and internal stable parts is largely controlled by a critical state of stress upon which either renewed failure or fault inactivation occurs. On this basis, we suggest that critical-taper analysis of wedges must be restricted to specific kinematic segments. Comparison of the experimental results with the Nankai accretionary wedge suggests that our interpretation also applies to natural convergent wedges. Moreover, we provide constraints for the selection of adequate granular analogue materials to simulate typical crustal rocks in natural convergent wedges.

Keywords: Analogue experiments; Material properties; Friction; Strength; Granular materials; Scaling; Critical-taper theory; Accretionary wedges; Orogenic wedges

1. Introduction

Critical-taper theory is a concept with a high potential to understand orogeny, owing mainly to its simplistic and straightforward way of linking the force balance of an orogen in selfsimilar growth mode to its bulk geometry, mechanical properties, and kinematics (Chapple, 1978; Davis et al., 1983). This approach has been successfully used to explain the mechanics of fold-and-thrust belts, forearc wedges as well as entire orogenic belts (Davis et al., 1983; Platt, 1986; Willett, 1992). Scaled analogue experiments with granular materials (e.g. sand), in particular, were able to link the internal structural evolution and related particle displacement field to the material properties, thereby yielding a first-order approach to understand the mechanics of different deformation styles that may be applied to nature (e.g. Malavieille, 1984; Huiqi et al., 1992; Lallemand et al., 1994b; Gutscher et al., 1996; Wang and Davis, 1996).

Despite this successful application of the critical-taper theory, it has been recognised that a more detailed mechanical analysis and description of experiments performed with scaled analogue materials fails to correctly explain predicted or observed geometries. The theoretical critical 'Coulomb Wedge' (Davis et al., 1983; Dahlen, 1984) may not adequately describe the deformation patterns of convergent non-cohesive sand wedges and their characteristic

* Corresponding author. Tel.: +49-331-2881313; fax: +49-331-2881370.

E-mail address: jo@gfz-potsdam.de (J. Lohrmann).

0191-8141/03/$ - see front matter © 2003 Elsevier Science Ltd. All rights reserved.
PII: S0191-8141(03)00005-1

convex topography (Mulugeta, 1988; Mulugeta and Koyi, 1992).

From critical-taper theory it follows that only three fundamental material properties control the critical wedge geometry, the internal kinematics, and stress regime of a wedge that remains at hydrostatic fluid pressure: internal and basal friction (μ_{int}, μ_b), and cohesion (C; Fig. 1a). Hence, an explicit understanding of the deformation processes and the discrepancies described above requires that specific attention needs to be given to the properties in analogue materials, so that they properly represent natural materials. The physical properties of dry granular materials, such as quartz sand, were investigated by several authors (Hubbert, 1937; Mulugeta, 1988; Huiqi et al., 1992; Lallemand et al., 1994b; Gutscher et al., 1996; Cobbold, 1999). From their results, average material properties are commonly assessed to determine an overall effective scaling factor and to describe the analogue material used—not resolving, however, the problem mentioned above. Based on the analysis of natural wedges by Zhao et al. (1986), Mulugeta and Koyi (1992) suggested that deformation-dependent variations of cohesion can cause a convex wedge shape and may be a key element to overcome the discrepancy between theory and experiment as cited above.

Recent, more detailed analyses on granular material behaviour suggested a refined treatment of analogue experiments (Krantz, 1991; Schellart, 2000). Accordingly, deformation behaviour for small normal stresses (0–400 Pa)—as is the case in common laboratory setups—is more complex than previously assumed and, in addition, internal friction also depends on rounding, sphericity, and grain size (Schellart, 2000). Krantz (1991) revealed that the preparation technique (sifted, poured or sprinkled) of the sand is decisive for internal friction and that the frictional properties differ significantly for fault initiation and for reactivated faults. This latter feature is well known from experiments performed on natural rocks (Brace and Byerlee, 1966; Byerlee, 1978; Paterson, 1978) and forms the basis for assessing the strength of the continental crust. This may be of major importance since critical-taper theory implicitly only uses one set of frictional coefficients. The assumption of constant frictional properties helps to estimate down-scaled material properties. However, this restriction may be an oversimplification, the consequence of which for analysis of experimental wedges has not been established. Accordingly, proper representation of natural systems in experiments must (a) identify the factors that control material properties and use these to choose materials according to the behaviour of natural rocks in the brittle field, and (b) based on these results, define a strategy that is appropriate to

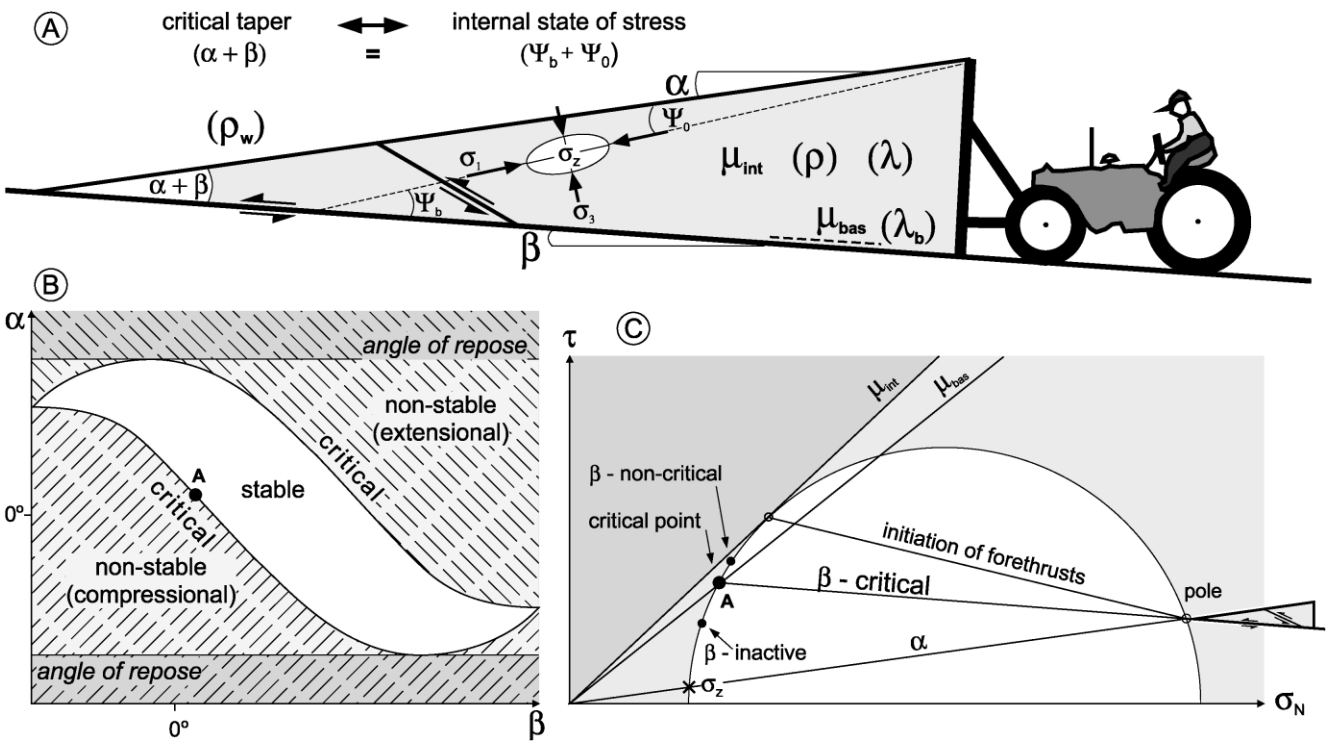

Fig. 1. (A) Convergent wedge and its controlling parameters: α—surface slope; β—basal dip; μ_{int}—coefficient of internal friction; μ_{bas}—coefficient of basal friction; λ—internal pore pressure ratio; λ_b—basal pore pressure ratio; ρ—density of rocks; ρ_w—density of seawater (σ_1—maximum principle stress; σ_3—minimum principle stress; Ψ_0—angle between σ_1 and surface slope; Ψ_b—angle between σ_3 and wedge base; after Davis et al., 1983). (B) α/β-diagram with indicated dynamical states of a convergent wedge with a specific ratio of friction (μ_{bas}/μ_{int}; after Dahlen, 1984). The point marks the wedge shown in (A). (C) Conventional Mohr-diagram of convergent wedges with indicated states of stress at the depth z (σ_z), determined from the basal dip (β) for a given surface slope (α). The point A marks an activated basal detachment of a critically-tapered wedge. Stresses determined by the second intersection with the Mohr circle of any line passing through the pole (pole construction method; Terzaghi, 1943) act on a plane oriented parallel to that line in physical space.

extend the analysis of accretionary wedges, fold-and-thrust belts, and orogenic belts.

In the present paper, we attempt to address these two issues with a mechanical-property analysis and a series of convergent sandbox experiments with a highly idealised setup. These experiments focus on the determined material properties and the associated kinematic evolution of thrust wedges. We first analyse the dependence of the mechanical properties of granular analogue materials (quartz sand) on standard handling techniques by shear tests. We then demonstrate the role of material properties that show variations during ongoing deformation and establish the potential of quartz sand to be used for scaled analogue experiments. Lastly, we will show how these results can be applied to the understanding of the mechanics of scaled analogue experiments by performing critical-taper analysis.

2. Theoretical background

The critical-taper theory shows that any orogen will evolve towards a dynamically steady state with a balance between material input and wedge taper (slope angle + basal dip) as well as with the mechanical properties of the wedge itself and its basal shear zone (Fig. 1a; Davis et al., 1983; Dahlen, 1984). Dynamic equilibrium of a wedge, as expressed by stable sliding of a wedge over its base without internal deformation, will only be affected by changes of its boundary conditions (e.g. its mechanical properties, material supply, amount of material eroded, etc.). Accordingly, a convergent wedge can exhibit three dynamic states (i.e. state of stress; Fig. 1b and c; Dahlen, 1984):

1. In the stable state, the wedge does not need to accommodate minor changes in its boundary conditions (e.g. its mechanical properties, material supply, amount of material eroded etc.) as long as these do not lead to a state of near-failure throughout.
2. At the limits of the stable state—the critical state—equilibrium is achieved between the basal traction, the stresses acting at the rear of the wedge and the frictional resistance of the wedge material and its base, i.e. the wedge is at failure throughout during slip over its base. Such a critically-tapered wedge is indicated by faults that are continuously at failure.
3. In the non-stable state, the wedge is in a sub-critical or supra-critical state and has to adjust its shape to a critical state by internal deformation, i.e. by shortening in the case of the sub-critical state or by extension in the case of the supra-critical state.

A wedge, which is in a critical state of stress, will grow self-similarly by adjusting its critical shape during material addition (or removal) by internal deformation. Strain rates are largest where modification of the wedge shape is caused by changed parameters, as the new parameters determine another critical taper, to which the wedge has to adjust. In fossil orogenic belts, this is obvious, e.g. from repeated reactivation of faults, formation of out-of-sequence faults, domains of diffuse wedge-internal deformation with second-generation fabrics, or from synconvergent extensional collapse of parts of the wedge.

The Coulomb Failure Criterion, as used in the critical-taper theory, defines the behaviour of Coulomb Wedges. In this context, a Coulomb-type material is defined to be non-cohesive and characterised by a linear stress-strain relationship, until failure occurs (Fig. 2a). Subsequent plastic deformation then proceeds under constant shear stress. The strength of such a material at failure, i.e. the peak strength, is equal to the strength during stable sliding. The coefficient of friction, therefore, depends solely on the strength at failure and the normal stress. However, mechanical experiments on natural rocks have established that a distinction must be made between the properties of an undeformed and deformed material (Brace and Byerlee, 1966; Byerlee, 1978; Paterson, 1978). Undeformed materials have higher strengths and higher friction coefficients than fractured materials (Fig. 2b). The strength of the latter is only controlled by the frictional strength of existent faults.

In agreement with this observation, wedge materials, such as natural rocks or granular analogue materials, show a more complex behaviour during the phase of plastic deformation than that described by the Coulomb Failure Criterion (Fig. 2b and c). Investigations of bulk solids have shown that granular materials display a complex strain-dependent behaviour (Vaid and Sasitharan, 1992; Chu, 1995; Schanz and Vermeer, 1996). They are characterised by elastic/frictional properties, with strain hardening prior to failure and subsequent strain softening, until a dynamically constant shear load is reached (Fig. 2c). This evolution is related to a compaction–decompaction cycle. Frictional coefficients derived from laboratory experiments show that a peak friction coefficient may be assigned to the initial yield strength of the samples, while a lower stable friction coefficient is linked to stable sliding (Han and Drescher, 1993; Anand and Gu, 2000). It should be noted that the stress-strain curves of natural rocks are comparable with those of granular materials. However, in the case of rocks, strain-hardening and strain-softening effects also depend on strain rate, temperature, effective stresses, and roughness of the sliding surface (e.g. Jaeger and Cook, 1969; Rutter, 1972; Scholz and Engelder, 1976).

Despite the more complex material behaviour of rocks, a 'Coulomb Rheology' may be used to describe the mechanical behaviour of the upper brittle crust on a regional scale (Davis et al., 1983). This has been justified from the observation that rocks are penetrated by fractures, microcracks and mechanical heterogeneities of any orientation (Sibson, 1974; Brudy et al., 1997). Failure by reactivation, therefore, will occur prior to attaining the peak strength related to undeformed rocks. Accordingly, stable sliding can be assumed to control the critical taper of a natural

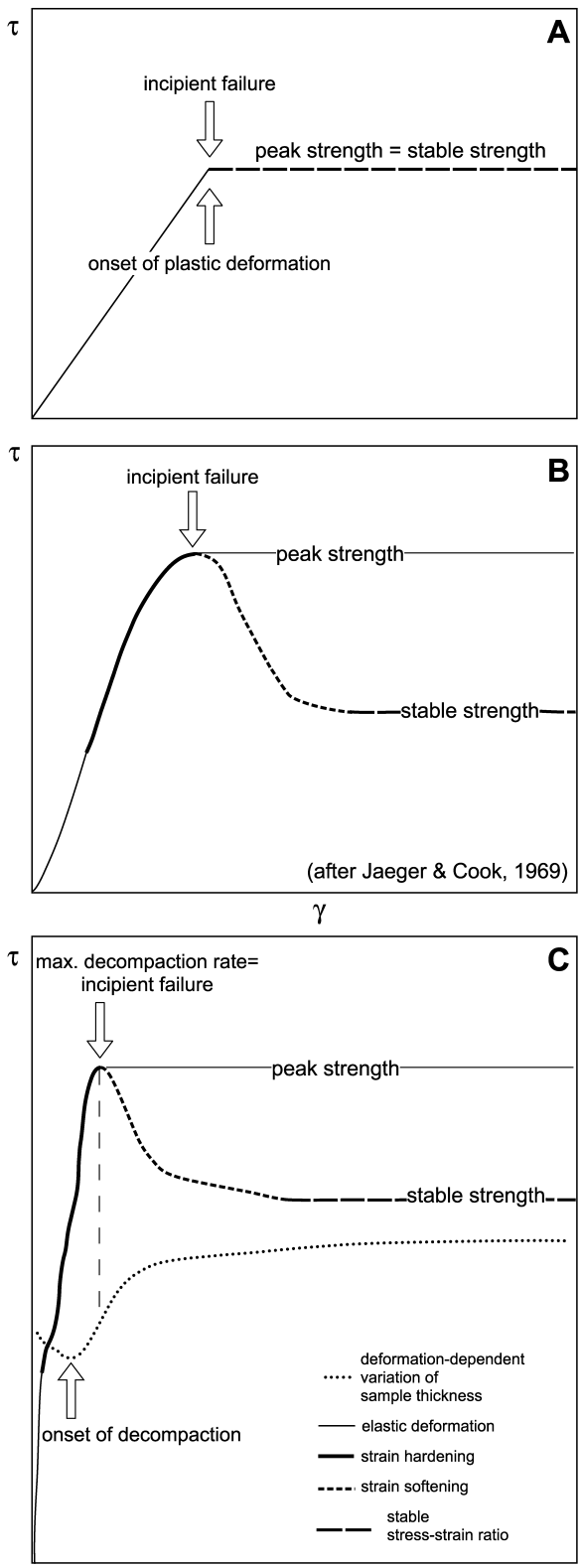

Fig. 2. Plots of shear-stress (τ) as a function of angular shear (γ) show that the material behaviour of (A) an ideal Coulomb-material is distinctly different from that of (B) natural rocks and (C) granular analogue material.

compressive wedge. The elastic/frictional behaviour of rocks with strain hardening and strain softening then can be substituted by that of an ideal cohesionless Coulomb-material for investigations on a regional scale.

In contrast, the simplistic assumption of a 'Coulomb Rheology' may not apply to the behaviour of granular analogue material (Krantz, 1991; Schellart, 2000). It might therefore not be justified to use granular materials to simulate the behaviour of the brittle upper crust. Also, the critical-taper approach may not adequately describe sandbox experiments. A solution to this problem lies with the identification of the basal and internal frictional properties of sand wedges and the potential consequences for the critical-taper approach to analogue models.

3. Material properties

3.1. Material characterisation

To evaluate the influence of internal and basal frictional strength on the evolution of sand wedges, the possible influence of all other material properties has to be excluded. Therefore, in all experiments performed in this study, we employed the same sand (S30T—Quaternary, glacial, almost pure quartz sand from Königslutter, Germany). This sand was washed and dried at high temperature by the distributing company, so that the finest fraction (<20 μm) was removed. Consequently, the size of the well-rounded, moderately-spherical grains varied between 20 and 800 μm. Grain-size distribution strongly skewed toward the larger sizes on a standard ϕ-plot with a maximum at 350–400 μm. To obtain materials with different properties, the sand was separated into different grain-size fractions and the shear apparatus was filled using two different methods; sifting and pouring (Table 1). In the following, the different sand fractions (poured or sifted) are named as 'sands'. In this study, sands were sifted from ca. 20 height with a rate of 130 cm^3/min. The poured sands were filled all at once from a height of ca. 10 cm into the apparatus. The mechanical properties of the different sands were measured with a modified Hubbert-type shear apparatus (Hubbert, 1951), which allows the determination of the ratio of normal stress to shear stress at failure (Fig. 3a). Strength at failure was measured by increasing the shear load until initial failure occurs. The mass (M_{crit} in Fig. 3) of the shear load was determined to calculate the internal peak strength. In a second step, the shear load was again increased until renewed slip in the sheared sand occurred. This provided the internal stable strength of deformed material. For the measurement of the material properties of the shear zone at the base of the sand layer, we employed a box, the bottom of which was attached to the basal material as used in the sandbox experiments (paper). This box was set on top of a thin layer of sand (Fig. 3b). The technique to measure basal

Table 1
Physical properties of sands obtained from S30T measured with the Hubbert-type shear box. Italic lines indicate the sands used for sandbox experiments. (ρ—density; ϕ_{peak}—angle of peak friction, μ_{peak}—coefficient of peak friction, C_{peak}—peak cohesion, ϕ_{stable}—angle of stable friction, μ_{stable}—coefficient of stable friction, C_{stable}—stable cohesion)

Sand type	Grain size spectra (μm)	Preparation method	Homogeneity of grain size distribution	Grain size	ρ (g/cm^3)	ϕ_{peak} (°)	μ_{peak}	C_{peak} (Pa)	ϕ_{stable} (°)	μ_{stable}	C_{stable} (Pa)
SIF	*<400*	*Sifted*	*Inhomogeneous*	*Fine grained*	*1.67*	*35.9*	*0.72 ± 0.01*	*28 ± 10.3*	*28.3*	*0.54 ± 0.02*	*83 ± 11*
SHF	*220–400*	*Sifted*	*Homogeneous*	*Fine grained*	*1.65*	*34.4*	*0.68 ± 0.02*	*49 ± 15*	*29.2*	*0.55 ± 0.02*	*75 ± 12*
SIC1	*>400*	*Sifted*	*Inhomogeneous*	*Coarse grained*	*1.67*	*31.8*	*0.62 ± 0.02*	*80 ± 25*	*27.6*	*0.52 ± 0.02*	*75 ± 16*
SIC2	<630	Sifted	Inhomogeneous	Coarse grained	1.73	33.6	0.67 ± 0.02	32 ± 11	27.6	0.52 ± 0.02	86 ± 24
SHC	400–630	Sifted	Homogeneous	Coarse grained	1.67	32.8	0.65 ± 0.02	45 ± 17	28.8	0.55 ± 0.01	72 ± 8
PIF	*<400*	*Poured*	*Inhomogeneous*	*Fine grained*	*1.54*	*23.5*	*0.44 ± 0.02*	*123 ± 13*	*27.6*	*0.53 ± 0.02*	*95 ± 24*
PHF	200–400	Poured	Homogeneous	Fine grained	1.5	25.0	0.47 ± 0.02	99 ± 18	27.6	0.52 ± 0.02	78 ± 21
PIC1	>400	Poured	Inhomogeneous	Coarse grained	1.54	26.2	0.49 ± 0.02	62 ± 22	27.4	0.52 ± 0.02	71 ± 22
PIC2	<630	Poured	Inhomogeneous	Coarse grained	1.53	27.5	0.52 ± 0.02	46 ± 17	29.3	0.56 ± 0.02	37 ± 11
PHC	400–630	Poured	Homogeneous	Coarse grained	1.51	28.8	0.55 ± 0.02	26 ± 14	28.5	0.54 ± 0.02	53 ± 15

peak and stable strength was the same as described for the internal properties.

To minimise error, these measurements were repeated up to six times using different normal loads for each sand (1.5–4 kg, in steps of 0.5 kg) and an experiment was repeated for each normal load three times. The coefficient of friction and the cohesion were then determined by linear regression analysis (Fig. 3c). For the coefficient of friction, standard error of all measurements was smaller than 0.02 (Table 1). Cohesion, however, can only be determined with a precision of ca. 30% with this method. Therefore, cohesion was also determined with a ring-shear tester (Schulze, 1994).

In addition, another error in the measurements of stable friction was introduced by measurement under static conditions, i.e. the fault plane is reactivated and not continuously active as e.g. often observed in sandbox experiments. Therefore, the results of these static measurements were confirmed by selected dynamic measurements performed in a ring-shear tester (Schulze, 1994), which measures the material strength during ongoing deformation. Two shear-load cycles were performed with the same normal load. The peak strength of the first cycle was used to calculate the peak friction, whereas the peak strength of the second cycle led to the stable static friction (i.e. the friction that was overcome at the moment of fault reactivation). The stable dynamic friction for continuously active faults was given by the constant strength during further deformation. Furthermore, these measurements allowed recording of deformation-dependent compaction and decompaction. The comparison of the two methods (shear box, ring-shear tester) showed that the measurements with the ring-shear tester are faster, more precise with a standard error smaller than 0.007 and provide more detailed results.

3.2. Results

Sand density was mainly controlled by the filling technique of the shear box. The densities of poured sands had a smaller range and were also significantly lower (1.5–1.54 g/cm^3) than those of the sifted sands (1.65–1.73 g/cm^3; Table 1). Whereas sifting generated more densely packed well-compacted sands, pouring always produced under-compacted materials. The better compaction of the sifted sands is ascribed to the slower filling velocity than pouring. During sifting, individual grains were repeatedly redeposited by the hit of newly dropped grains until all grains were ideally packed. For both filling techniques a homogeneous sand always had a lower density and higher porosity than an inhomogeneous sand.

Since the cohesion of the sands was very low (<130 Pa; Table 1) when compared with the normal stress acting in the ring-shear tester, Hubbert-type shear box, and the sandbox experiments (>1000 Pa) the critical shear stress was mainly governed by the friction. Moreover, the cohesion did not correlate with either sand density or degree of compaction. Therefore, this study mainly focuses on friction. From this

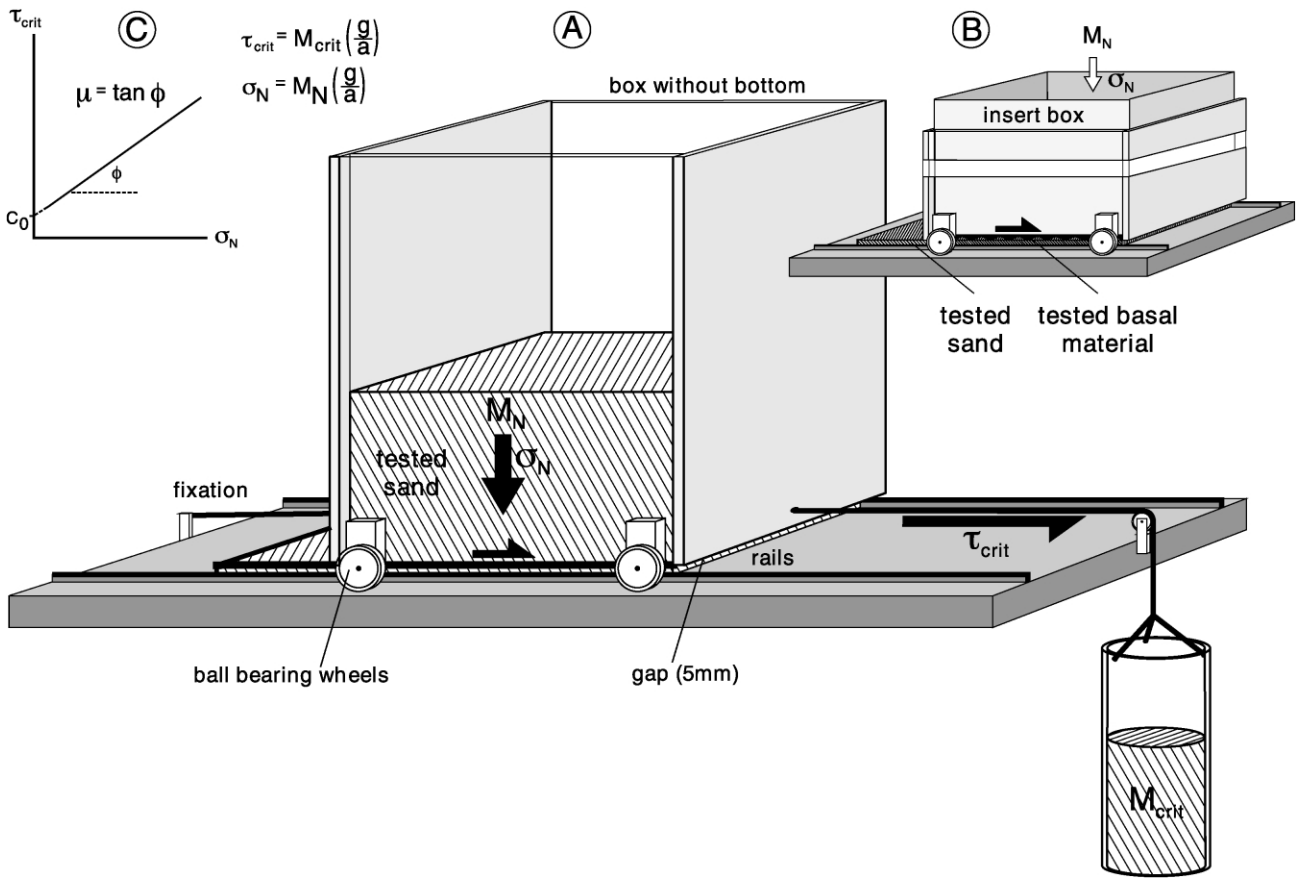

Fig. 3. Hubbert-type shear box (A) to determine internal friction and cohesion of granular materials; (B) to determine the basal friction between granular materials and the materials of the basal interface. (C) Shear stress as function of normal stress for a granular analogue material. The slope gradient of the line represents the friction angle (Φ). The intersection of the line with the ordinate represents the cohesion (C_0). (μ—coefficient of friction; M_N—normal load; M_{crit}—critical mass of shear load; σ_N—normal stress; τ_{crit}—critical shear stress, g—acceleration due to gravity, a—area of fault plane.)

point onwards friction is always given in terms of the dimensionless coefficient of friction and named *friction* throughout.

Peak internal friction was a function of the filling technique of the shear box. Pouring the sand results in significantly lower peak friction (0.43–0.55) than sifting (0.62–0.72; Fig. 4a and c). These ranges do not overlap, revealing that friction was mainly controlled by compaction and density. In addition, peak internal friction was affected by grain size and degree of homogeneity, resulting in minor variation of this parameter. In sifted sands, peak friction increased with grain-size heterogeneity and decreasing grain size. In contrast, poured sands showed increasing peak friction with increasing grain size and homogeneity.

There was a remarkable difference between peak and stable frictions (Fig. 4b and d). Stable friction of the different sands did not show the well-defined separation between the two techniques of shear box filling. All sands investigated in this study had nearly the same internal stable friction (0.52–0.56) with no systematic influence by grain-size homogeneity or spectrum.

Basal friction was only measured for those sands that were used in the sandbox experiments (SIF, SHF, SIC1, PIF; Table 2; Fig. 4e and f). The values were lower than the respective internal frictions, while the trends were comparable with the values of peak internal friction and stable internal friction. The inhomogeneous sifted sand with small grain size (<400 μm) had the highest peak basal friction (SIF: 0.53 ± 0.02), whereas the equivalent poured sand had the smallest peak basal friction (PIF: 0.38 ± 0.02). The stable basal friction ranged from 0.45 to 0.55.

The results of the dynamic measurements performed in the ring-shear tester confirm the results of the static measurements for the internal material properties with respect to the

Table 2
Physical properties between the basal interface and sands used in the sandbox experiments. (ϕ_{peak}—angle of peak friction, μ_{peak}—coefficient of peak friction, ϕ_{stable}—angle of stable friction, μ_{stable}—coefficient of stable friction)

Sand type	Grain size spectra (μm)	ϕ_{peak} (°)	μ_{peak}	ϕ_{stable} (°)	μ_{stable}
SIF	<400	28	0.53 ± 0.02	27.4	0.52 ± 0.02
SHF	220–400	26.7	0.50 ± 0.02	25.5	0.48 ± 0.02
SIC1	>400	27.1	0.51 ± 0.02	27.8	0.53 ± 0.01
PIF	<400	21	0.38 ± 0.02	24.1	0.45 ± 0.01

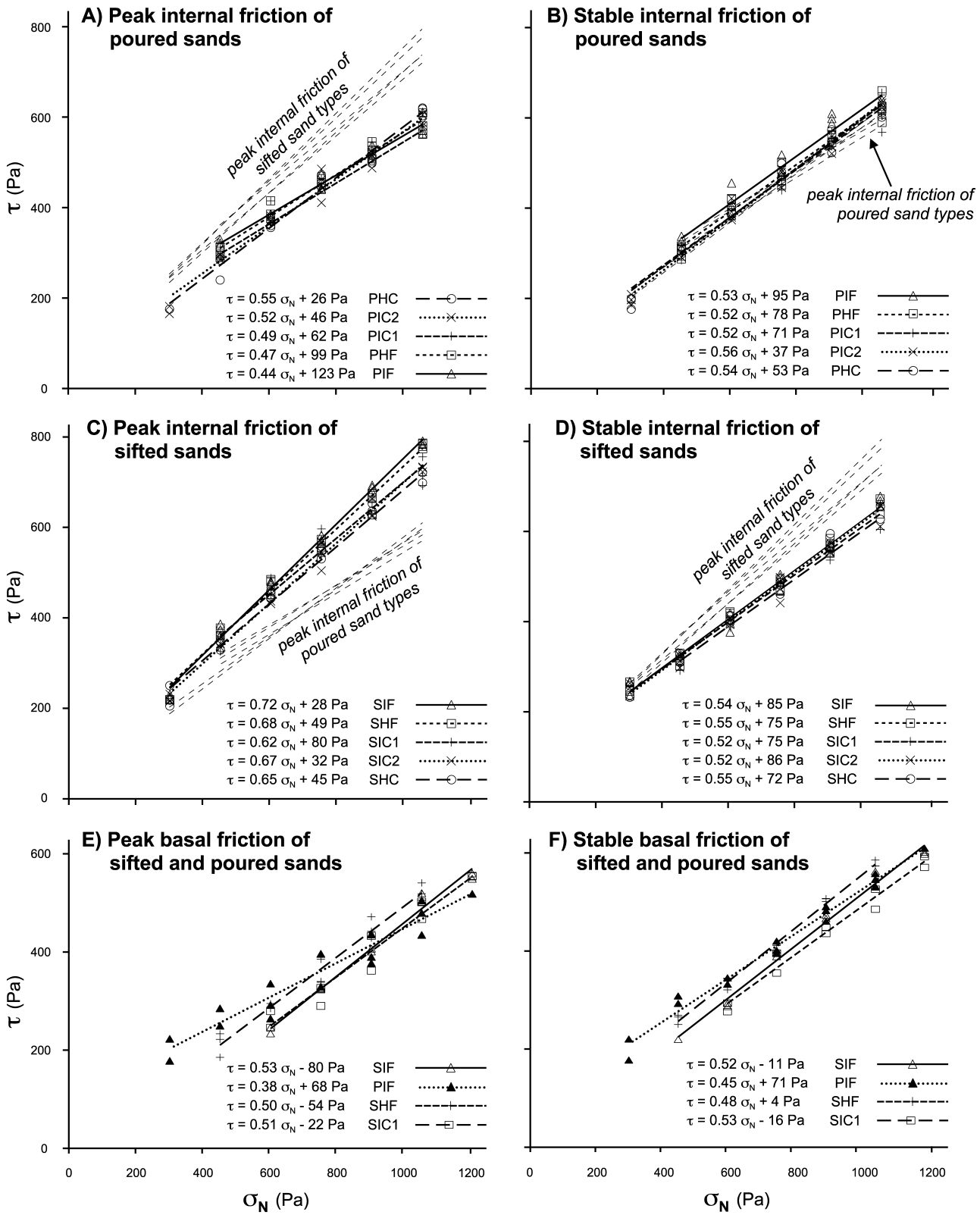

Fig. 4. Shear stress (τ) plotted as a function of normal stress (σ_n) for tested sands in the Hubbert-type shear box. Internal and basal friction and cohesion are derived from linear regression analyses of these data (Fig. 3c). For errors see Tables 1 and 2 and Section 3.

peak strength of undeformed materials. However, the dynamic measurements indicated that stable dynamic strength of deformed materials was always lower than stable strength, in the case of static measurements of deformed material. For the basal shear zone, test runs showed that the friction for stable sliding in identical materials with an identical filling technique is some 0.07 lower for dynamic measurements than static measurements. This significant difference can probably be ascribed to repeated stops and reactivation of slip imposed by the setup of the shear box, whereas the stable strength of the dynamic measurements is related to ongoing shear zone development.

Comparison of peak and stable strength of various sands showed that poured sands had a small ratio of peak strength to stable strength, whereas this ratio was high for sifted sands (with equivalent ratios of peak versus stable friction; Fig. 5). In addition, dynamic strength measurements performed in the ring-shear tester showed a transient strength development of all samples during increasing shear deformation along with a systematic compaction–decompaction cycle. Early diffuse deformation was associated with sample compaction, followed by a stage of dilatancy of the granular material during the pre-failure deformation. Increasing plastic deformation, during increasing shear load, was associated with plastic hardening of the samples in this stage (Fig. 5). Failure, i.e. formation of a localised shear zone, is inferred to occur near peak strength and peak decompaction rate, as also observed in the analysis of granular materials (Han and Drescher, 1993; Anand and Gu, 2000). Subsequent strength drop of the material and the transition to stable sliding was associated with a decreasing decompaction rate.

The degree of compaction and strain hardening prior to pervasive deformation mainly depended on the filling technique (Fig. 5). Well-compacted sifted sands only exhibited minor compaction during this stage. In contrast, undercompacted poured sands showed a high degree of compaction. In all sands, the onset of plastic deformation occurred before peak strength was reached. The well-compacted sifted sands showed substantial dilatancy during deformation, whereas the undercompacted poured sands only showed minor decompaction in the localised shear zone. Thus, sifted and poured sands possessed quite a different decompaction capability. This resulted in nearly the same stable friction for all sands once the stage of stable sliding was reached. Moreover, three of the tested sands showed a slight strain hardening (SIC1/PIF) or slight strain softening (SHF) during more advanced stages of shearing.

The measurements reported here suggest that the filling technique of the shear box has a major influence on internal peak friction, confirming the results of an earlier parameter study (Krantz, 1991). Furthermore, as our measurements reveal internal stable friction of the different sand types to be quite uniform, we conclude that stable friction is not influenced by the method of filling the shear box, nor are grain size or homogeneity of any relevance. Moreover, the sands tested in this study show no compaction-dependent variation of cohesion, as has been shown for the sand used by Mulugeta (1988) and Mulugeta and Koyi (1992). In addition, the results of the ring shear tests reveal that sands typically used as analogue material show transient, deformation-dependent frictional properties with elastic-plastic behaviour, as well as initial strain hardening and strain softening.

4. Sandbox experiments

4.1. Experimental setup

Four scaled sandbox experiments with a highly idealised setup were performed to study the influence of material

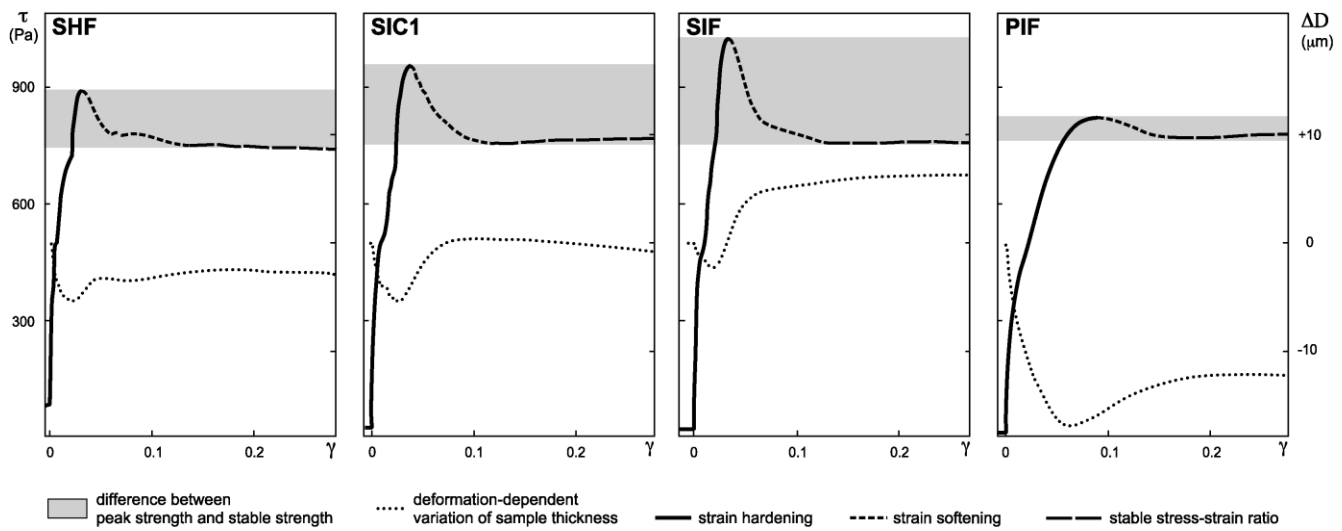

Fig. 5. Plots of shear-stress (τ) and variation of sample thickness (ΔD) as a function of angular shear (γ) of different sands. The difference between peak and stable strength is related to the initial degree of compaction of the tested sands.

properties on the kinematics, growth mechanisms, and internal deformation patterns of sand wedges. Only the sand types were varied between the individual experiments. The scaling of the experiments to nature was calculated considering the cohesion and material density (scaling factor: $[C/\rho g]_{nature}/[C/\rho g]_{model}$; Hubbert, 1937; Lallemand et al., 1994a; Koyi, 1997; Schellart, 2000), as the experiments were performed under normal gravity. For the mean values of cohesion (marine sediments: 5–20 MPa; Jaeger and Cook, 1969; Hoshino et al., 1972; analogue materials used: 30–130 Pa) and density (marine sediments: 2300–2500 kg/m^3; analogue materials used: 1500–1700 kg/m^3), a scaling factor of 10^5 was calculated.

The criteria to select the sands for the sandbox experiments were: filling technique, grain size, distribution of grain size, as well as peak internal friction. Because different sands overlay the basis, which was held identical in all experiments, this resulted in relative different basal properties.

A glass-sided box (200 cm × 20 cm) with a basal dip of 0° was used for the experiments (Fig. 6). A conveyor belt, topped with the same paper as used in the measurements for basal friction, was moved by an electric motor to converge the overlying sand layer (thickness: 3.5 cm) towards the rigid backwall (velocity: 4 cm/min). Thin marker layers and triangular-shaped markers of coloured sand within the sand layer enabled observation of the internal wedge structure and particle paths, which were continuously recorded. The coloured sand had a slightly higher cohesion (120 Pa) and nearly the same internal peak friction as sifted sands ($\mu_{int\ peak} = 0.7$). Tests established that a small volume of sand with properties differing from the bulk sand properties had no influence on the fault geometry and kinematics of sand wedges.

4.2. Results

In the following, the common and contrasting features of the sand wedges are emphasised to evaluate the influence of the varied properties of the sand. The common features indicate the general evolution of a convergent sand wedge in a frontally-accretive mode, whereas the contrasting features refer to the influence internal friction had on the kinematics and dynamics of the convergent sand wedges.

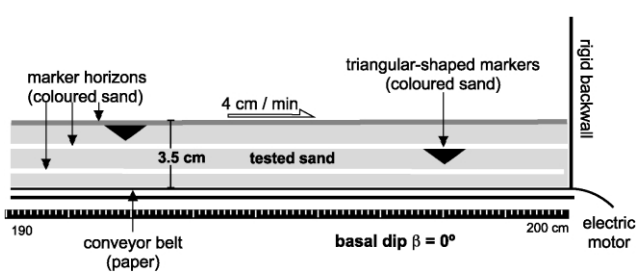

Fig. 6. Setup of the sandbox experiments. Only the tested sand was varied from one experiment to another.

4.2.1. Common features

The shortening of the incoming sand-layer resulted in a sand wedge with fore- and backthrusts in a frontally-accretive mode. A steady-state wedge geometry was achieved after all the segments of the wedge, which are defined in the following, were assembled. In all experiments, the steady-state wedge shape was characterised by up to three domains, each with a different surface slope (from the wedge tip to the rear; Fig. 7a):

1. the frontal surface slope changed its inclination (i.e. transient surface slope), but never reached the steepness of the surface slope of the adjacent segment,
2. a steeply-inclined surface slope with constant inclination over time, and
3. a shallow and constant surface slope.

The boundary between the latter two segments was in some cases indistinct, or even formed a gradual transition zone.

These three domains coincided with domains of unique structural styles and, in particular, with different kinematics (Fig. 7b):

1. In the frontal-deformation zone (FDZ), the incoming material formed new thrust slices. Such a thrust slice belonged to the FDZ until it was incorporated into the adjacent (more steeply tapered) wedge segment. In the first step of initial faulting, a pair of conjugate fore- and backthrusts broke through the incoming sand-layer. After 1–3 cm of convergence, backthrusting ceased, when it reached the tip of the previously-formed thrust slice. Subsequently, the hinterland-dipping thrusts were the dominant faults. This segment included up to three imbricates.
2. The frontal-imbrication zone (FIZ) was located next to the FDZ. The FIZ contained several thrusts, all of which were continuously active, maintaining a constant surface slope as the wedge volume increased. The more internal forethrusts in the FIZ were back-rotated during piggy-back translation.
3. In the internal-accumulation zone (IAZ), the adjustment of the wedge geometry to the continuously-increasing wedge volume was produced by occasional reactivation of some or all of the earlier-formed thrusts. This deformation rather caused vertical uplift than horizontal shortening. Fault planes were further back-rotated and eventually became inactive. The IAZ was separated by the leading out-of-sequence thrust (LOT) toward the FIZ.

In a single thrust slice, most deformation took place along the base (Fig. 7c). However, a small component of

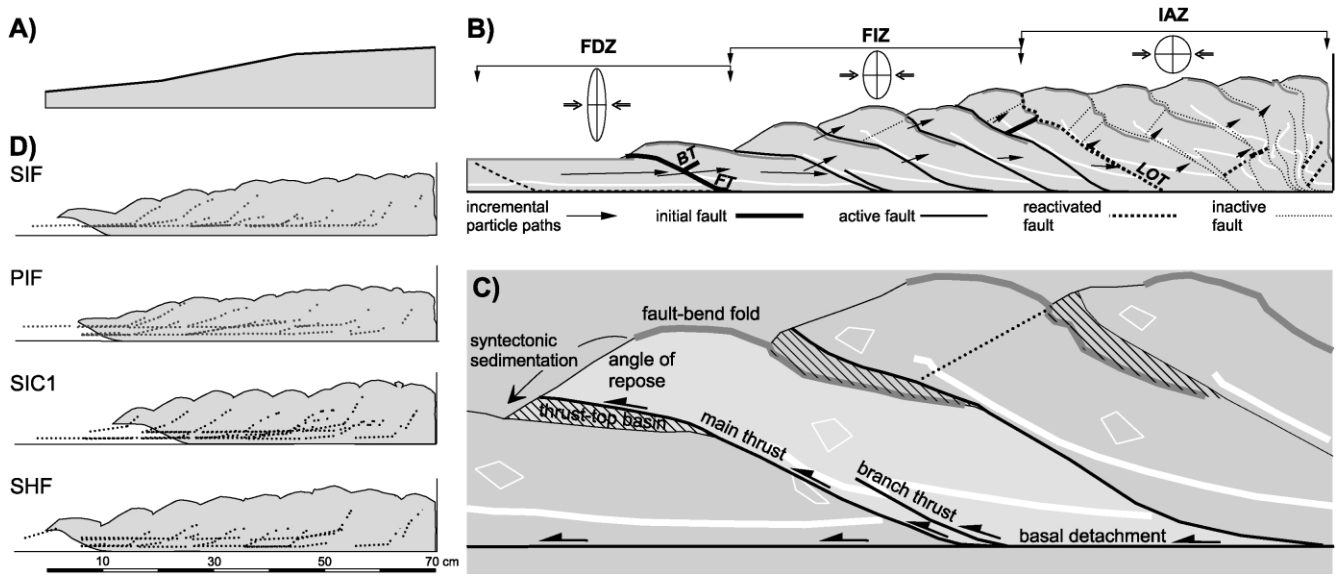

Fig. 7. Common features of the convergent sand wedges consisting of different sands. (A) The overall wedge geometry is characterised by three domains with different surface slopes. (B) The kinematic segments (FDZ—frontal-deformation zone; FIZ—frontal-imbrication zone, IAZ—internal-accumulation zone) show typical internal kinematics, horizontal shorting rates and incremental particle paths (FT—forethrust; BT—backthrust, LOT—leading out-of-sequence thrust). (C) Internal kinematics of an individual thrust slice with formation of a subsequently overthrust 'thrust-top-basin'. (D) Total displacement fields in the sand wedges do not show any substantial difference.

internal strain occurred in two strain patterns:

1. localised shear displacement along distinct branch thrusts, and
2. diffuse intergranular deformation.

In all experiments, bulk particle paths were nearly identical (Fig. 7d). Incremental analysis of the displacement field exposed three well-defined domains of mass transfer, from the wedge tip to the rear, which correlated to the domains of similar surface slope and internal kinematics described above (Fig. 7b). These incremental displacement fields also demonstrate that the wedges were kinematically segmented. Material that moved through the FDZ showed the largest horizontal displacement and most variable uplift (i.e. most variable inclination of particle paths). As material moved into the FIZ, horizontal displacement diminished, with only moderate uplift, where both became continuously smaller toward the rear of this domain. In the IAZ, material velocities slowed down further. This zone comprised the smallest horizontal displacements and the steepest inclination, when compared with the other domains.

4.2.2. Contrasting features

Wedge tapers were determined by measuring the slope of the line linking the tips of the thrust sheets (wedge taper $= \alpha$, since $\beta = 0°$) of the three kinematic segments every 10 cm of convergence.

Systematic variation in wedge geometry of the different sand wedges was only observed in the surface slope of the FIZ (Fig. 8). Here, the surface slopes varied between 7.8 and 11.3°. In addition, the PIF surface slope showed a decrease from 7.8° at the front to 5.2° at the rear. The SIC1 surface slope had a large error in its mean value. This error was caused by measuring the taper in this experiment at different stages of new imbricate incorporation. In the other experiments (SIF, PIF, SHF), taper measurements were always performed at the same stage of imbricate incorporation, which prevented this ambiguity.

In addition, the shortening required to reach steady state varied from one experiment to another. In the experiment with PIF, the steady-state phase was attained most rapidly (after 30 cm convergence), whereas the experiments with SIC1 and SHF reached this stage only after 60 cm of convergence.

The main difference in the kinematics of the different sand wedges was observed in the IAZ (Fig. 9). The faults were either reactivated occasionally (SIC1, SHF), or were persistently inactive except for reactivation of the LOT (SIF; Fig. 9). This different kinematic behaviour of the IAZ caused different modes of wedge adjustment. Occasional reactivation of all the out-of-sequence thrusts (SIC1, SHF) led to an episodic or cyclic wedge adjustment, which was also related to distributed deformation in the IAZ. Reactivation of only the LOT, without segment-internal deformation (SIF), led to localised and episodic wedge adjustment. The PIF sand wedge lacked an IAZ and a well-defined slope segmentation. Here, all thrusts were continuously active, and, accordingly, showed no rearward limit of the FIZ.

The sand wedges also differed with respect to the internal strain of the thrust slices. Comparison of strain between the experiments requires a segment, which is in steady state and shows the same kinematics in all experiments. Therefore,

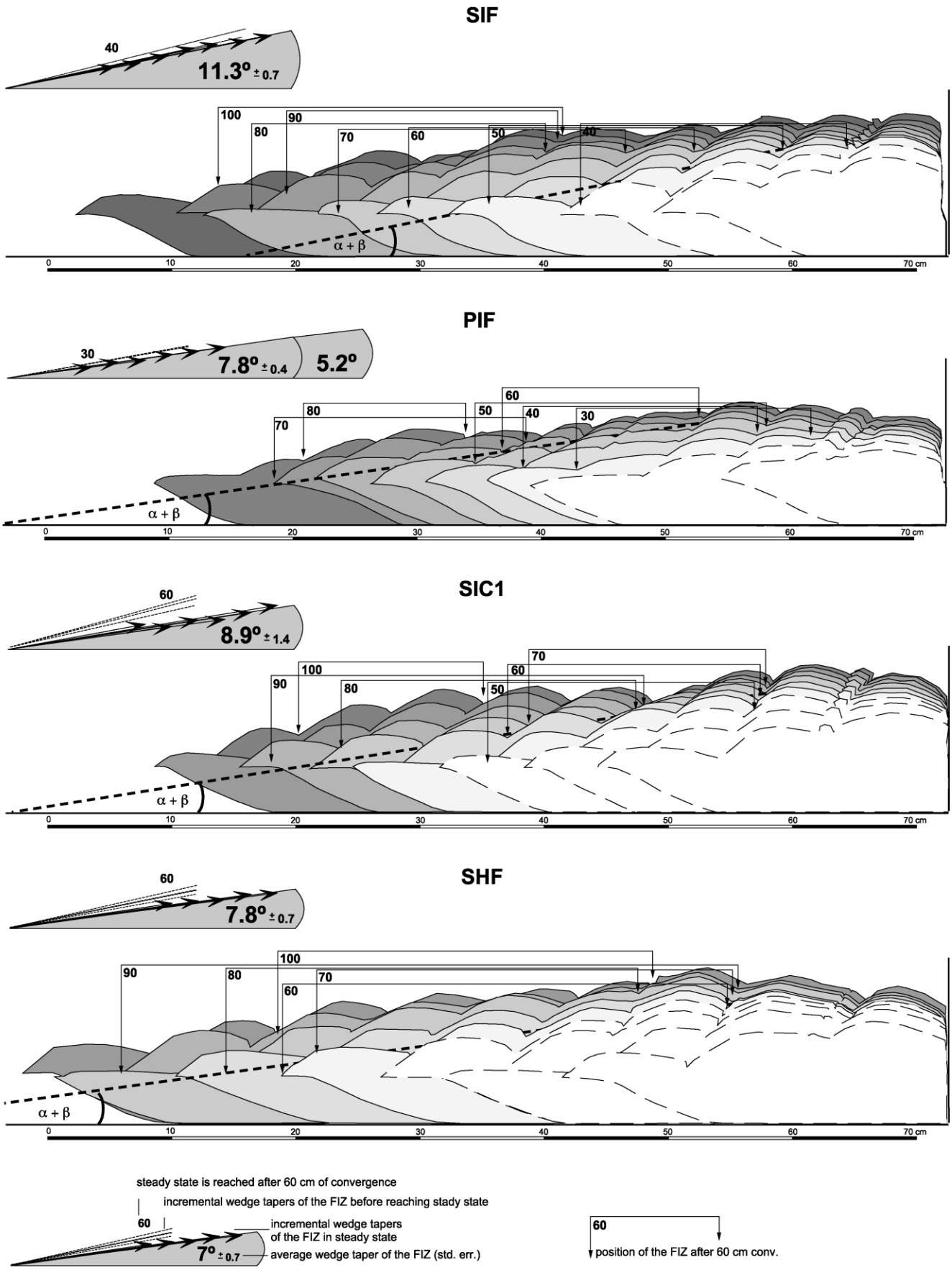

Fig. 8. Wedge geometry plotted after every 10 cm convergence. Dashed lines indicate the geometries before the wedge has reached steady state; solid lines indicate the steady state geometries. The wedge taper of the frontal-imbrication zone (FIZ) during its evolution is determined from these diagrams.

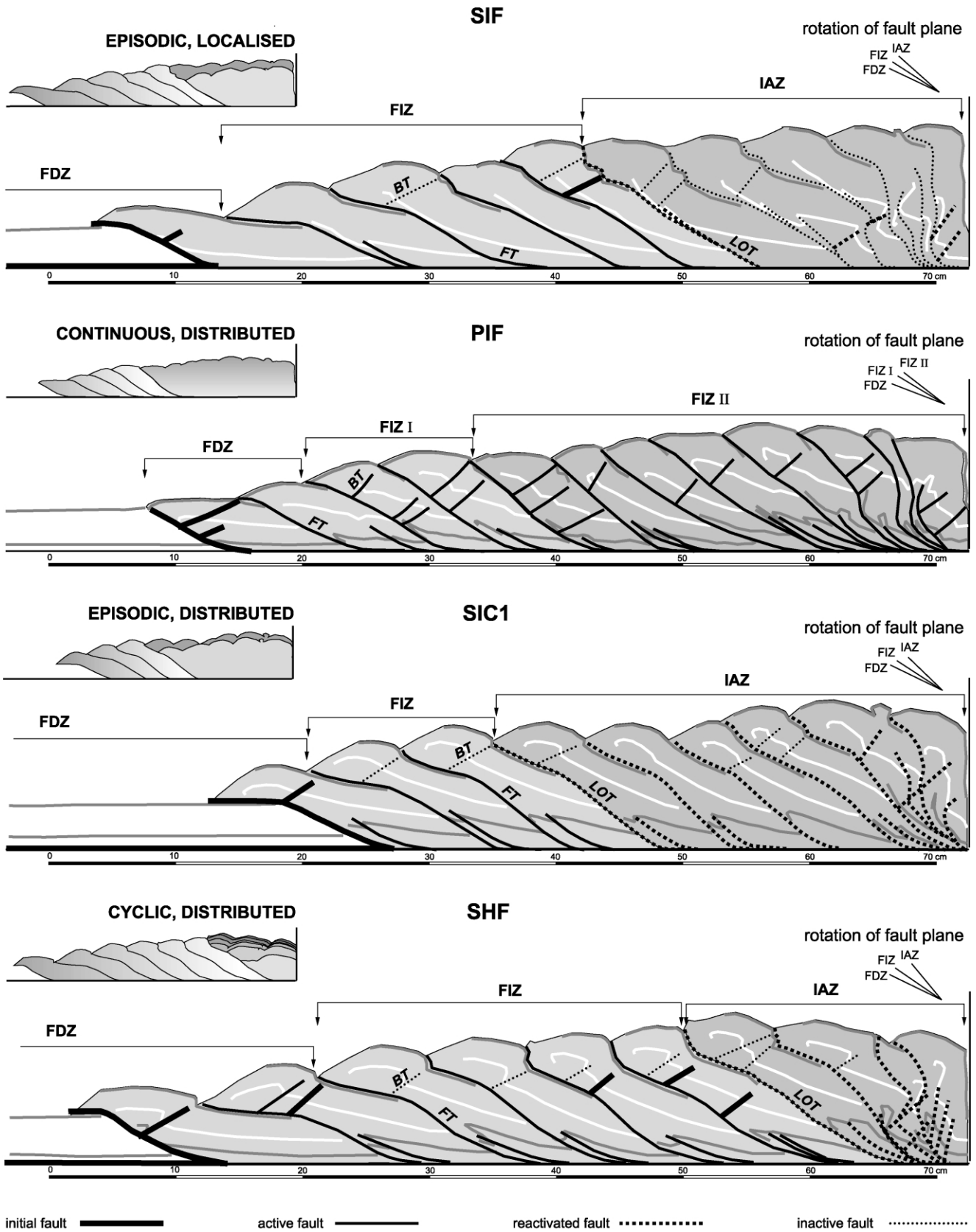

Fig. 9. Kinematic features of the convergent sand wedges. The kinematics and modes of wedge adjustment (see sketches at the left) of the internal-accumulation zone (IAZ) is different in each experiment, whereas the kinematics of the other wedge segments (FDZ—frontal-deformation zone; FIZ—frontal-imbrication zone) are similar (FT—forethrust, BT—backthrust).

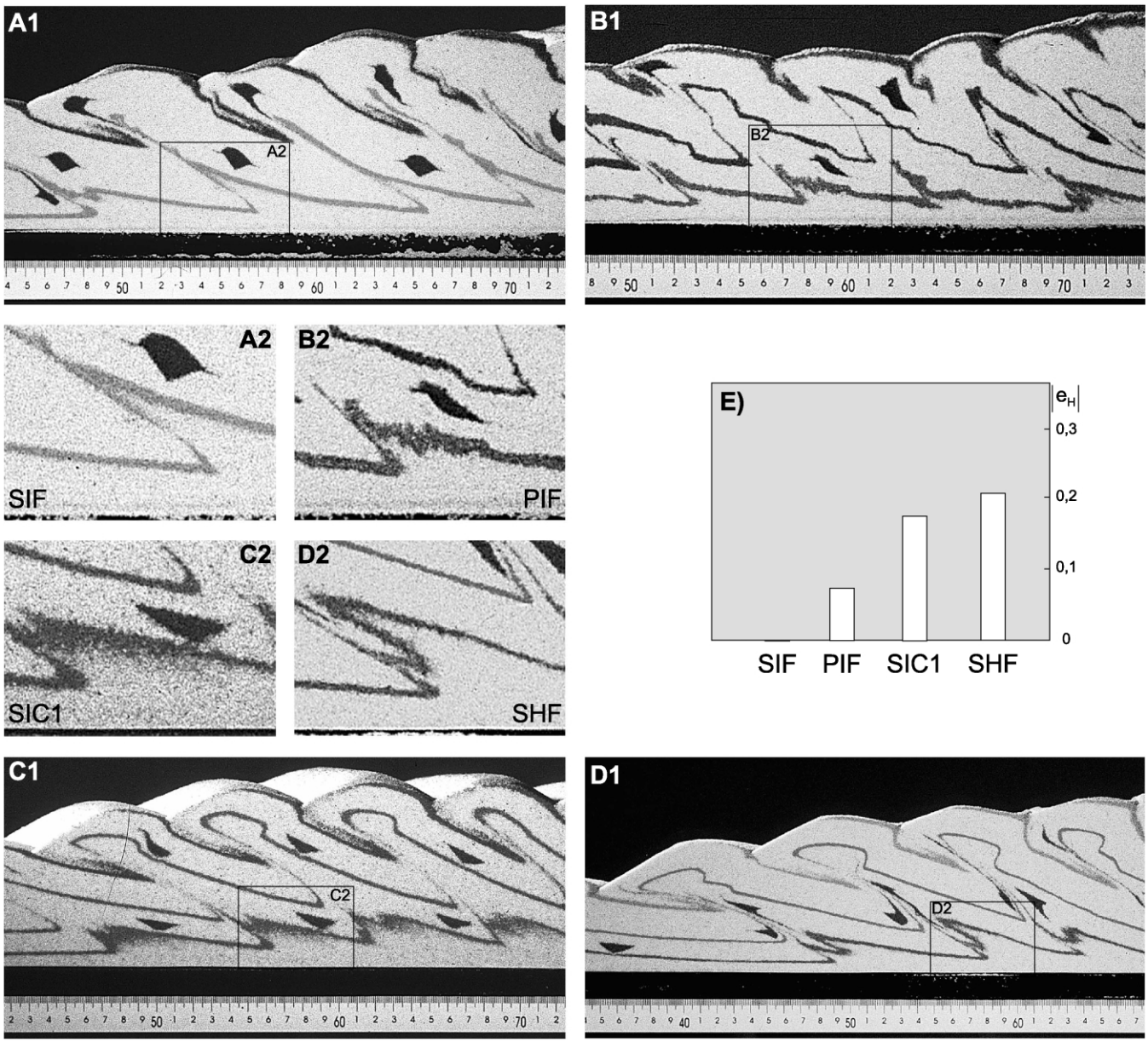

Fig. 10. Detail ((A1)–(D1) not on scale; (A2)–(D2) at the same scale) shows a different degree of diffuse deformation within the imbricates. The photographs of the different experiments show ((A)–(D)) the total diffuse deformation accumulated in the frontal-deformation zone and in the frontal-imbrication zone. (E) Horizontal shortening (e_H) due to diffuse deformation of an imbricate during its evolution in the frontal-imbrication zone.

the only segment that is suitable for this strain comparison is the FIZ. The internal strain varied with respect to localisation and amount (Fig. 10). In well-compacted sands with high internal friction (SIF), strain was exclusively accumulated by localised deformation at distinct branch thrusts (Fig. 10a). In all other sands, deformation occurred by a combination of localised strain and diffuse, intergranular deformation (Fig. 10b–d). In addition, the amount of this diffuse deformation differed (Fig. 10e). It is important to notice that the initially undercompacted PIF material showed only minor diffuse deformation in the FIZ, whereas the well-compacted sifted sands SHF and SIC1 exhibited substantial diffuse deformation in this segment.

The features of the FDZ indicated a non-stable state of this segment, which kept a sub-critical state, due to constant and high material flux through the deformation front. The FIZ, in contrast, was at failure throughout, and therefore, in a critical state of stress. This is inferred from continuously-active thrusts and a stable wedge taper during material addition. The IAZ only occasionally showed pervasive failure due to ongoing material addition and was therefore in a stable state of stress. In contrast to previous literature, our results show that convergent sand wedges are kinematically and dynamically segmented, indicating that only a part of the wedge, depending on material properties, is critically tapered and suitable for quantitative critical-taper analysis.

5. Mechanical analysis

The material and kinematic analyses described above show that mechanic analysis of the sandbox experiments must focus on two aspects: the role of peak versus stable friction in wedge evolution and the coexistence of various segments with different tapers, namely in the FIZ and IAZ.

The quantification of internal and basal friction shows that there are two possible end member values (peak and stable dynamic) for internal and basal friction that may control the wedge taper. The results of sandbox experiments suggest that each kinematically-defined segment may have specific frictions. The faults in the FIZ were continuously-active thrusts. The friction of the fault material, accordingly, was probably near the internal stable dynamic friction. Also, the basal interface below the FIZ was continuously active, suggesting that stable dynamic friction was also attained here. This hypothesis is evaluated through critical-taper analysis.

The critical-taper analysis made use of the results from the previous analysis and from measurements in the Hubbert-type shear box (Table 1). The stable friction measured with the static approach was corrected by the empirically-derived value from dynamic measurements with the ring-shear tester (see Section 3.2) and used as stable dynamic friction. The critical-taper analysis was performed on the FIZs of the sand wedges made of SIF, PIF, and SHF. The wedge, which consisted of SIC1, could not be used for the critical-taper analysis, as the error of the measured wedge taper was too large to expect a reasonable result (see Section 4.2.2).

The critical-taper equation (Eq. (1)) allows the iterative calculation of the friction value of the basal detachment below the FIZ, as all other variables are given. The equation for non-cohesive critical Coulomb wedges for dry systems is defined by Dahlen (1984) as:

$$\beta = \frac{1}{2}\arcsin\left(\frac{\sin\phi_b}{\sin\phi}\right) - \frac{1}{2}\phi_b - \left[\frac{1}{2}\arcsin\left(\frac{\sin\alpha}{\sin\phi}\right) - \frac{1}{2}\alpha\right] - \alpha \quad (1)$$

where α is the surface slope, β is the basal detachment dip, ϕ is the internal friction, and ϕ_b is the basal friction.

Basal friction values were calculated assuming first stable dynamic internal friction and then peak internal friction, and were then compared with the basal friction values obtained from the shear-box tests.

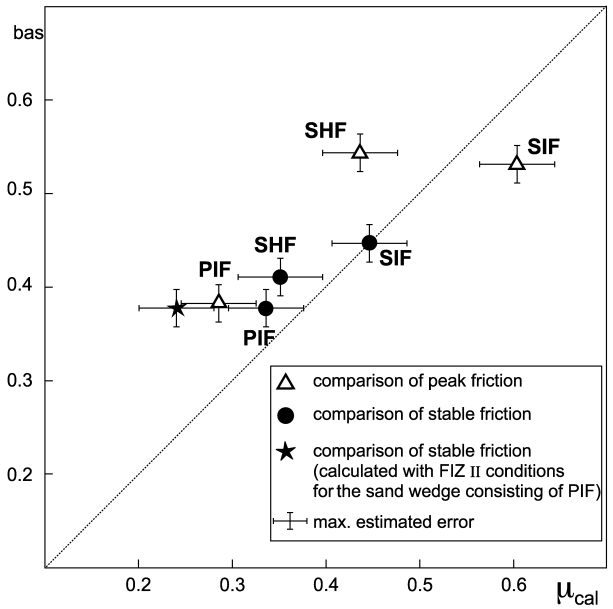

Fig. 11. Comparison of calculated values of the coefficient of basal friction (μ_{cal}) employing Eq. (1) with measured values of the coefficient of basal friction (μ_{bas}). Dotted line indicates the perfect fit of measured and calculated values.

The analysis showed that only the stable dynamic friction (basal and internal) lead to results reasonably consistent with the experimental observations (Fig. 11). Here, the wedge that consisted of SIF showed a perfect match between the measured and calculated basal friction. In contrast, the measured absolute values of basal friction slightly exceeded the calculated absolute values of the PIF and SHF wedge. With respect to the estimated maximum error (from measurements of surface slope and friction), only a minor difference between measured basal friction and calculated basal friction (<0.01) was still observed for the wedge that was built of SHF, with measured values slightly higher than theoretical values. This systematic deviation is probably because constant material accretion in the experiments continuously altered the perfectly critical taper.

Depiction of the above-described relationship in Mohr Diagrams (Fig. 12) shows the stresses required for contemporaneous active slip at the wedge base and on the internal thrusts of the FIZ, i.e. the critical state. The constraints used for construction were the failure curves as measured (for peak and stable dynamic internal friction of wedge material, and its base), the wedge tapers measured in the sandbox experiments, and the dip of the trailing internal

Fig. 12. Mohr diagrams using the pole projection method (P—pole; Terzaghi, 1943) show the state of stress required for the critically-tapered frontal-imbrication zone (FIZ) at the depth z (σ_z) in the sand wedges consisting of (A) SIF, (B) PIF, (C) SHF. The constraints used for construction are the failure curves as measured for peak internal ($\mu_{peak\ int}$), stable internal friction ($\mu_{peak\ int}$) and for stable basal friction ($\mu_{stable\ bas}$), the wedge taper ($\alpha + \beta$) measured in the sandbox experiments, and the dip of the trailing internal forethrust (FT) of the frontal-imbrication zone (FIZ). The Mohr-diagrams are accompanied by the stress-strain curves of the respective material to illustrate the strength development in the shear zones during deformation under the load conditions of the frontal-imbrication zone (FIZ). (μ_{cal}—basal friction calculated with internal stable friction; τ—shear stress; normal stress—σ_n; angular shear—γ).

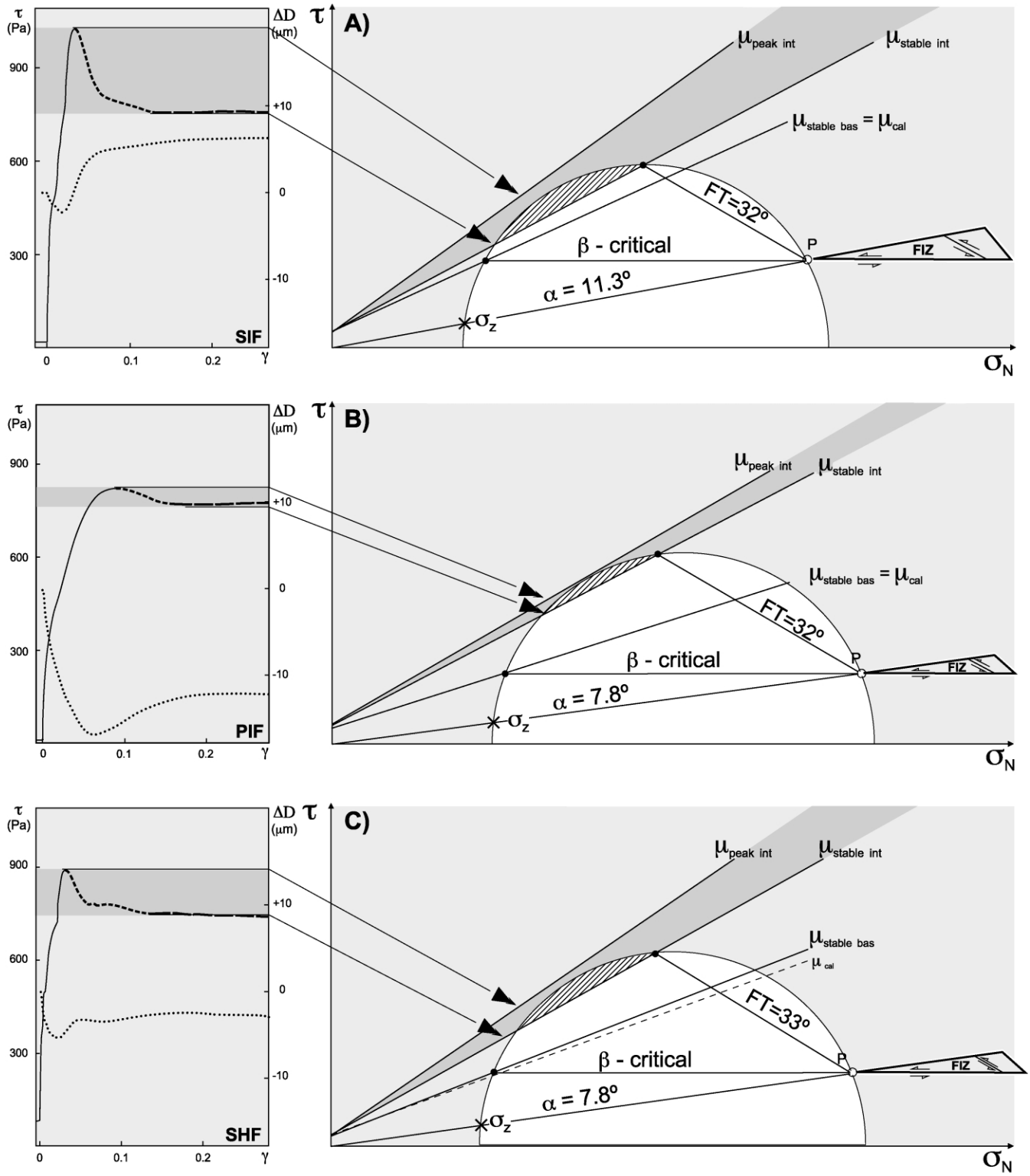
τ (Pa)
ΔD (μm)
900
600
300
+10
0
-10
SIF
0
0.1
0.2
γ
A)
μpeak int
μstable int
μstable bas = μcal
FT=32°
β - critical
P
FIZ
α = 11.3°
σz
σN
PIF
B)
α = 7.8°
SHF
C)
FT=33°
strain hardening
strain softening
stable strength
deformation-dependant variation of sample thickness
difference between peak and stable strength
area of potential orientations of active forethrusts

thrust of the FIZ (FT in Fig. 12). This part of the FIZ is the key for understanding the mechanical conditions for deformation, since its analysis illustrates the extreme conditions under which critical behaviour occurs.

As inferred from the results shown in Fig. 11, the SIF wedge (Fig. 12a) shows a very close match between the measured and calculated basal friction. This result is derived with the assumption that bulk wedge strength in this part of the FIZ is determined by the stable dynamic friction of the trailing active thrust. To maintain slip on this thrust after its back-rotation, the differential stress must increase. In this case, thrusts of various orientations can be reactivated if the material has reached stable sliding conditions (dashed field in Fig. 12). However, the peak strength of unfailed SIF material was not reached, and therefore no new structures formed. This example can, accordingly, be seen to support the aforementioned hypothesis of stable dynamic friction as the key property controlling critical taper.

Since the PIF experiment showed a continuously decreasing taper across its critical FIZ, we separately analysed the frontal part and the rear part. The frontal part showed similar behaviour to the SIF wedge with respect to friction dependence, and with respect to fault reactivation without formation of a new fault generation (Fig. 12b). Closer inspection, however, reveals minor internal deformation of the imbricates of the PIF material during active fault slip in the FIZ. Therefore, wedge adjustment in the FIZ was achieved by internal localised fault slip and minor diffuse grain scale deformation. As shown by the critical taper analysis, however, the wedge taper was controlled by the frictional properties at stable sliding conditions.

The shallower surface slope (5.2°) in the rear part of the PIF experiment results in an underestimation of the basal friction (0.24) at constant internal friction or an overestimate of the internal stable friction (0.73) at constant basal friction (Fig. 11). The latter value is well below the peak frictional strength of undeformed material. These results indicate that the friction values as measured are not valid for the more internal parts of this sand wedge.

Whilst the stress-strain curve of the SHF material was similar to that of the SIF material, the sand wedge consisting of SHF showed substantial diffuse deformation in the FIZ (see Fig. 10). Similar to the result shown in Fig. 11, the Mohr Diagram demonstrates a minor difference between the calculated and the measured basal friction for stable sliding (Fig. 12c).

The mismatch between the measured and calculated basal friction (PIF, SHF) is proportional to the increase in diffuse deformation. Thus, mechanical analysis leads to results inconsistent with frictions measured with the standard measuring techniques applied here. In these cases, critical-taper analysis leads to meaningless results. Accordingly, it can neither be ascertained for this material whether frictional properties remain stable with increasing deformation, nor whether fault friction controls wedge taper.

In summary, we conclude from the analysis of the FIZ of all wedges that taper and internal kinematics were predominantly controlled by the frictional properties of faults that have reached the state of stable sliding. Peak frictional strength did not directly influence the dynamic state.

6. Discussion

6.1. Transient wedge mechanics

Segmentation of the wedges, as identified from kinematic analysis, is not directly explained by the mechanical analysis presented above, and even appears to be in conflict with measured friction values in the case of the PIF wedge. A more detailed analysis of the states of stress of the rear parts of the sand wedges provides a more straightforward explanation. The experiments show that slip on some of the faults in the FIZ proceeds at differential stresses higher than necessary to overcome the frictional strength of optimally-oriented faults that have reached the state of stable sliding (FT in Fig. 12). This is a consequence of antithetic rotation of the faults into a mechanically less-favourable position once they have left the FDZ and entered the FIZ (Fig. 9). As a consequence, differential stresses required for slip increase towards the boundary between the FIZ and IAZ, i.e. therefore also the bulk strength of the wedge increases in this direction.

An important implication of this is that the boundaries of the FIZ, i.e. the segment limits within the wedge, are controlled by key mechanical boundary conditions: the boundary between the FDZ and the FIZ is a zone of minimum wedge strength since it shows an optimally-oriented leading fault, once it has reached the stage of stable sliding. Wedge strength increases due to fault rotation and strain hardening by diffuse deformation toward the boundary of the FIZ to the IAZ. Here the wedge strength evolves to a point where two possible effects can occur:

1. Slip on a rotated fault may eventually require differential stresses beyond the upper bound of plastic hardening of the thrust sheets near peak frictional strength of the material. Subsequent failure will then produce second generation faults crosscutting the earlier structures with a stress drop and a renewed transition to stable sliding. This should result in weakening of the bulk wedge strength and an equivalent increase in taper.
2. Peak strength is not reached and rotated faults are inactivated, because convergence is entirely taken up by the basal shear zone, which fails throughout. Accordingly, deformation in the wedge will cease, leading to a

transition into a stable state of stress below the current bulk wedge strength.

Thus, the horizontal length of the FIZ and FDZ are controlled by a deformation-dependent strength threshold (i.e. bulk wedge strength), reached after active faults have rotated through a critical angle.

In agreement with this argument and critical-wedge theory, the decrease in wedge taper of the IAZ must be due to a decrease of the frictional strength ratio between the basal detachment and the wedge material. We consider that the influence of the rigid backwall—which was similar in all experiments—is not important for the variable wedge taper in the IAZ at distances larger than experiment thickness, because there is a lack of a systematic relationship between the width and number of thrust slices at this distance. This increase in frictional strength ratio could be due to three aspects:

1. Since the friction of wedge-internal faults controls wedge taper, transient increase in stable dynamic friction can potentially cause a decrease in wedge taper. However, the material analysis in the ring-shear tests does not support the assumption that stable dynamic friction changes relevantly.
2. Similarly, weakening of the basal shear zone by a deformation-dependent process was not observed, nor could a load-dependent change in friction be confirmed. Ring-shear tests and the variable normal load (by a factor of as much as 1.5; from 1200 to 1800 Pa) at the downdip end of the FIZ–IAZ boundary in the experiments described here, show no significant change of friction at pressures above 200 Pa, similar to the results of Schellart (2000).
3. The only remaining explanation for the low taper of the IAZ and its kinematic properties is an increase in bulk wedge strength which, as argued above, could be due to progressive fault-rotation and associated plastic hardening in the thrust sheets as proposed by Mulugeta (1988). The reactivation of the faults in the stable state of stress requires fluctuation of the differential stresses above the frictional strength threshold, as for instance expected from discontinuous material addition to the IAZ.

The observed inconsistencies between measured and calculated basal friction for the rear segment of PIF wedge, require that material properties vary during such experimental runs. Transient, i.e. deformation-dependent changes of properties, apparently occurred in several instances: material analysis has established an elastic-plastic material behaviour with a strain-hardening and strain-softening cycle during initial diffuse deformation and fault formation (see Section 3.2)—a behaviour that is well known in soil mechanics (e.g. Schanz and Vermeer, 1996) but has not as yet been considered in geodynamic analogue simulations. This short-term transient effect, however, only affects fault material in the FDZ. After slip of a few millimetres, all materials reach the phase of stable sliding found to be the relevant property controlling the critically-tapered segments. This phase may exhibit a long-term transient change of friction. As hinted by the stress-strain curves in Fig. 12, minor changes may occur, both in terms of weakening or of strengthening, by a few percent. This effect again only affects the faults and is considered negligible.

More importantly, changes of mechanical properties that are related to initially undercompacted materials, e.g. PIF material, may be relevant (see compaction curves in Fig. 12). To maintain slip on the progressively-steepening faults in the entire actively-deforming zone of the PIF experiment, differential stresses must steadily increase to exceed the equally-increasing wedge strength. Because of the small initial difference between peak and stable frictional strength of PIF material and the absence of newly formed out-of-sequence faults, this necessitates an increase of the peak frictional strength of the material within the thrust sheets (Fig. 13). This is probably achieved by progressive compaction and deformation of the initially-undercompacted material during initial shear zone evolution in the FDZ. This transient deformation-dependent increase in peak friction is, at present, not quantitatively accessible, and can only be estimated by inference.

In undercompacted sands (e.g. PIF), it is probable that bulk compaction and peak friction increase equally with increasing deformation (see Section 3.2). At the same time, friction within faults converges toward a similar average

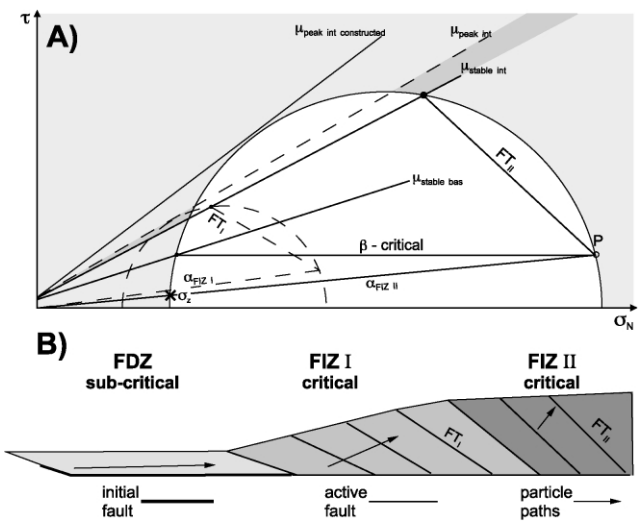

Fig. 13. (A) Schematic Mohr-diagram (as in Fig. 12) for the sand wedge consisting of PIF to illustrate the different state of stress in the rearward part of the FIZ (FIZ II—solid lines) compared with its frontal part (FIZ I—dashed lines). This diagram suggests a transient peak frictional strength ($\mu_{peak\ int\ constructed}$) within the imbricates. The constructed value for peak frictional strength is only semi-quantitative, as the influence of the rigid backwall is not considered in this schematic diagram. (B) For orientation, the general geometry of the sand wedge.

value, independent of the material type. Accordingly, with increasing deformation all materials should show behaviour typical of sifted sands, with high differences between peak and stable frictional strength, and an equivalent deformation localisation. Based on the semi-quantitative analysis of wedge-internal frictional strength from Fig. 13, we infer that the peak friction of undercompacted sand increased and reached the peak friction of the well-compacted SIF material during the initial compaction phase.

A key consequence of this argument is that the bulk strength of a particular, critically-tapered wedge segment is neither identical to the frictional strength measured from deformed materials for stable frictional sliding, nor to the peak strength of undeformed materials. Moreover, the occurrence of two or more different critically-tapered segments in a single wedge implies that a critical-taper analysis of such wedges cannot be performed with average values of material properties extrapolated from experimental data. Consequently, critical-taper analysis requires that the different kinematic wedge segments as well as the stages of the development of bulk wedge strength are identified.

Several researchers had identified segments by structural style and kinematics in natural convergent wedges (e.g. Nankai, Moore et al., 2001; Barbados, Zhao et al., 1986; Sunda, Kopp et al., 2002). In the next section we compare the Nankai accretionary prism with the segmentation of convergent sand wedges and discuss the applicability of our experimental results to nature.

6.2. Comparison with nature

The Nankai accretionary prism off SE Japan, which is one of the best investigated accretionary wedges on earth, shows evidence of segmentation due to bulk wedge-strength increase by rotation of fault planes (Fig. 14). Previous studies showed that the Nankai accretionary prism is separated into domains of unique kinematics (i.e. proto-thrust zone, imbricate thrust zone, frontal out-of-sequence thrust zone, large thrust-slice zone in Fig. 14 (Aoki et al., 1982; Ashi and Taira, 1992; Moore et al., 2001)). Although these domains do not correlate in all instances with the kinematic segmentation, as defined in this study, the natural and experimental wedges show some first-order agreements:

1. The turbidites of the protothrust zone are characterised by a strong decrease of porosity due to diffuse horizontal shortening and show distributed brittle deformation (Moore et al., 2001). These features correlate with those observed during the onset of deformation in the FDZ of the convergent sand wedges.
2. From the front to the rear, the taper of the imbricate thrust zone of the Nankai prism decreases with increasing rotation of thrust planes (Morgan et al., 1995; Moore et al., 2001). This coincides with the transition from the FIZ to the IAZ of the experimental wedges and supports the argument that the increase of bulk wedge strength is caused by thrust rotation.
3. The kinematics and geometry of the frontal out-of-sequence thrust zone of the Nankai accretionary prism are mainly a consequence of the onset of basal accretion (Moore et al., 2001). Thus, no part of the purely frontally-accretive sand wedges correlates with this part of the Nankai wedge.
4. The large thrust-slice zone of the Nankai accretionary prism is characterised by active out-of-sequence thrusts, which crosscut strongly-rotated thrusts of the first generation (Ashi and Taira, 1992; Moore et al., 2001). We suggest that these are the features of an IAZ in which bulk wedge strength achieves peak strength of undeformed material, as the first generation of thrusts reached a less-favourable orientation and new thrusts had to be initiated.

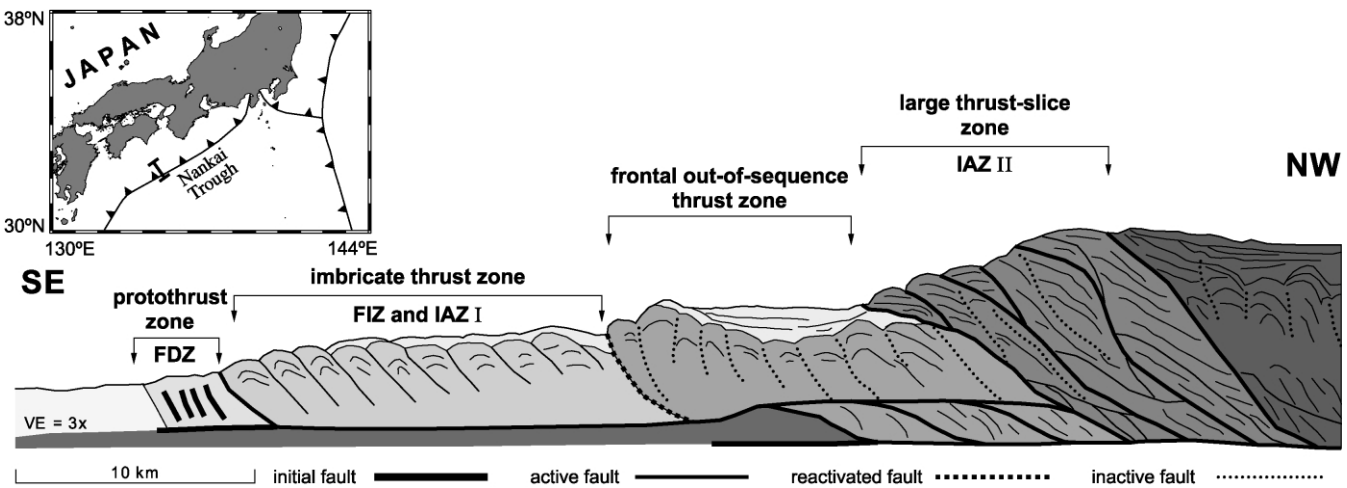

Fig. 14. Cross-section of the Nankai accretionary prism based on a schematic interpretation of seismic line 141-2D of ODP Leg 190 (Moore et al., 2001) with indicated fault kinematics. The major portion of the incoming sediment sequence is offscraped and frontally accreted, whereas the lower portion is basally accreted. The kinematic segmentation of the sandbox experiments is comparable with those parts of the Nankai wedge that are built by frontal accretion.

This comparison suggests that the results of the sandbox experiments may be able to explain the kinematic segmentation in natural wedges. Moreover, we expect that segmentation in natural wedges may be affected by additional aspects, such as variation in dip of the basal detachment, changes of rock properties by variation of cohesion (Zhao et al., 1986), fault sealing, mineral reactions, changes in pore pressure, and formation of anisotropic fabrics. However, the investigations of ODP Leg 190 (Moore et al., 2001) show that variation of basal dip, fault sealing, and mineral reactions do not influence the Nankai wedge.

Deformation or load-dependent changes in cohesion, in particular, have been invoked to explain the convex shape of natural and of analogue wedges (Zhao et al., 1986; Mulugeta and Koyi, 1992). The underlying assumption, however, is that of an ideal Coulomb-material with deformation-independent friction and accordingly, deformation-independent bulk material properties controlling the wedge. This study, in contrast, shows that the taper of individual segments in a critical and stable state of stress is entirely controlled by the friction of faults, because the frictional strength of granular materials during stable sliding is always lower than the peak strength of the undeformed material. Transient, deformation-dependent material properties within the thrust sheets only determine to which degree the faults may be rotated without becoming inactive. Accordingly, increasing cohesion can only play a role in the latter aspect and, indirectly, support an increase in rearward bulk wedge strength. To have an effect on the taper of a wedge, fault material must also be affected by cohesion increase. While this may occur in natural systems (by solution–precipitation processes and fault sealing, etc.), no evidence is available to support this inference for faults in analogue materials. The convex shape of convergent analogue wedges cannot simply be the consequence of an increase of the cohesion of the undeformed slice material. We expect a contribution of the latter aspect in natural wedges (as suggested by Zhao et al., 1986), but emphasise that here again the friction of fault materials—including their cohesion—is the key element controlling the taper and strength of wedges.

6.3. Analogue materials and natural rocks

Applicability of the arguments derived from the sandbox experiments to natural convergent wedges also strongly requires that natural rocks behave similarly to the used analogue material. Although more diverse, stress-strain curves of rocks are very similar to the stress-strain curves of the investigated sands (Jaeger and Cook, 1969; Paterson, 1978). At a larger scale moreover, the shape of the strength curve of faults in the brittle upper crust derived from laboratory tests matches the presented results for large sand samples (Fig. 15; Marone, 1998). Both, the brittle crust and the analogue materials, exhibit elastic/frictional plastic

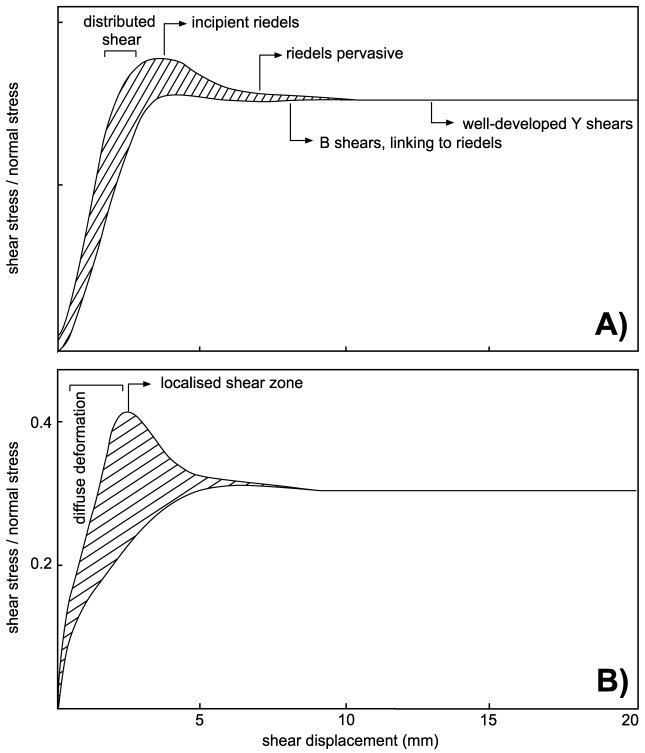

Fig. 15. (A) Sketch of a stress-strain curve during shear zone evolution in the upper brittle crust (after Marone, 1998); (B) sketch of a stress-strain curve for granular analogue material (hatched area—range of initial stress-strain behaviours, which are controlled by the degree of compaction).

material behaviour with an initial strain-hardening and strain-softening cycle.

The proper choice of analogue material is required to reproduce the overall wedge geometry of the individual kinematic segments in natural wedges, as well as to allow the comparison of their internal deformation patterns and kinematics. The relevant features are the initial difference between peak and stable frictional strength, long-term transient evolution of the fault itself and deformation-dependent evolution of the peak frictional strength of the material. However, even in the brittle field, natural rocks will invariably experience a variety of other processes that may cause transient mechanical behaviour. It should be noted, that the scaling of these various transient mechanical phenomena and its establishment in natural rocks, as well as in analogue materials, is an as yet unresolved problem (Paterson, 2001). In consequence, the identification of general similarities is the only viable strategy at present.

Brittle upper crustal rocks, from the results presented in this paper, are best represented by sifted, inhomogeneous, fine-grained sands (similar to SIF or SIC2). Unlithified, incompletely-compacted sediments with a low ratio of peak frictional strength to stable dynamic strength are best represented by poured sand, whereas sediments with a high strength ratio may react like sifted homogenous sand. Typical low porosity basement rocks show a continuous increase in strength during the

stable-sliding phase (Paterson, 1978). These rocks are best simulated by sifted inhomogeneous, coarse grained sands such as SIC1, which also exhibit a slight strain hardening during advanced stages of shearing. However, the stress-strain curves of this analogue material and the basement rocks are significantly different during initial failure. Consequently, a comparison of the experimental results with this sand to nature is only possible, if the investigated processes are independent of initial failure, e.g. like deformation processes in the FIZ or IAZ. Correlation in all cases, is however, dependent on two aspects:

1. The stress-strain curves of the analogue materials only image the mechanical evolution of fault material and not that of the surrounding material.
2. Mechanical properties of the analogue material are measured at sample scales similar to those used in the scaled analogue experiment itself. Data from natural rocks, however, represent small samples, the properties of which cannot directly be extrapolated to scales of friction-controlled orogenic wedges.

7. Conclusions

Our investigations show that the dynamics of convergent sand wedges can only be correctly described if a more complex material behaviour than previously assumed is considered. Sand exhibits an elastic/frictional plastic behaviour with transient strain hardening prior to failure and subsequent strain softening until the onset of stable sliding at constant friction. Although more diverse, stress-strain curves of natural rocks are very similar to the stress-strain curves of the sands investigated here. This confirms that sand can be considered a suitable analogue material for the simulation of crustal deformation in the brittle field.

The influence of preparation techniques on the friction of granular analogue materials, as well as friction of the basal detachment, are responsible for kinematic and dynamic segmentation of convergent sand wedges. Based on kinematic analysis, only parts of a wedge are critically tapered. Critical-taper analysis for individual wedge segments, whether in a critical or a stable state of stress, leads to a good agreement between theoretical prediction and measured friction values in the case of localised wedge-internal deformation (however, only a critically tapered segment allows complete quantitative evaluation).

As a result, the strength of critically-tapered wedge segments is mainly controlled by the frictional strength of the faults that have reached the state of stable sliding. While this allows a mechanical analysis based on the Coulomb Failure Criterion, it requires unambiguous identification of the critical state of stress within a specific segment. This is readily achieved in analogue experiments, but may pose problems in natural wedges where the distribution of seismicity, GPS strain, and continuous deformation of growth structures in syntectonic depositions may be the only reliable indicators of continuous failure. Moreover, the occurrence of two or more critically-tapered segments in a single wedge implies that a critical-taper analysis of such wedges cannot be performed with average values of material properties extrapolated from experimental data. In consequence, the critical-taper analysis requires identification of the different kinematic wedge segments, as well as of the specific stages of the development of frictional strength.

In convergent sand wedges, bulk wedge strength is not constant, as a consequence of progressive fault rotation into mechanically less-favourable orientations and associated plastic hardening in the thrust sheets by pervasive deformation. Bulk wedge strength increases toward the rear and influences the wedge segmentation. Segments in a critical state of stress are separated from stable segments (with all other conditions kept constant) by a strength limit. At this limit, the condition for continuous slip on previously established and rotated faults is exceeded, resulting in either inactivation of the fault with discontinuous reactivation or in renewed failure.

In undercompacted materials, peak strength of the material must increase as a consequence of pervasive deformation and bulk compaction. This deformation-dependent transient property shifts the position of the strength limits that control the wedge segments toward the rear. In such cases, the taper may continuously decrease, resulting in a convex geometry, although it is critical throughout. Also, mechanical properties predicted from taper analysis in these cases increasingly diverge from experimentally-obtained data, supporting the inference of deformation-dependent transience. Standard measuring techniques for these properties establish only the long-term development of shear-zone properties and, so far, do not allow the quantification of the friction of intervening material.

Moreover, the occurrence of two or more critically-tapered segments in a single wedge implies that a critical-taper analysis of such wedges cannot be performed with average values of material properties extrapolated from experimental data. In consequence, the critical-taper analysis requires identification of the different kinematic wedge segments, as well as of the specific stages of the development of frictional strength.

Acknowledgements

This study was carried out within the SP D6, Sonderforschungsbereich 267, financially supported by the Deutsche Forschungsgemeinschaft. We thank Mark Handy and Georg Dresen for constructive comments on an earlier version of the manuscript. Special thanks to Dave Tanner for correcting the English. We are grateful to Dan Davis and

an anonymous reviewer for helpful remarks and careful reviews. Technical assistance in the lab came from Günter Tauscher and Birgit Michel.

References

Anand, L., Gu, C., 2000. Granular materials: constitutive equations and strain localization. Journal of the Mechanics and Physics of Solids 48 (8), 1701–1733.

Aoki, Y., Tamano, T., Kato, S., 1982. Detailed structure of the Nankai Trough from migrated seismic sections. In: Watkins, J.S. Drake, C.L. (Eds.), Studies in Continental Margin Geology. AAPG Memoirs 34, pp. 309–322.

Ashi, J., Taira, A., 1992. Structure of the Nankai accretionary prism as revealed from IZANAGI sidescan imagery and multichannel seismic reflection profiling. Isl. Arc 1, 104–115.

Brace, W.F., Byerlee, J.D., 1966. Stick-slip as a mechanism for earthquakes. Science 153 (3739), 990–992.

Brudy, M., Zoback, M.D., Fuchs, K., Rummel, F., Baumgaertner, J., 1997. Estimation of the complete stress tensor to 8 km depth in the KTB scientific drill holes; implications for crustal strength. In: Haak, V., Jones, A.G. (Eds.), The KTB Deep Drill Hole. American Geophysical Union, Washington, DC. Journal of Geophysical Research 102, pp. 18, 453–18,475.

Byerlee, J., 1978. Friction of rocks. Pure and Applied Geophysics 116, 615–626.

Chapple, W.M., 1978. Mechanics of thin-skinned fold-and-thrust belts. Geological Society of America Bulletin 89, 1189–1198.

Chu, J., 1995. An experimental examination of the critical state and other similar concepts for granular soils. Canadian Geotechnical Journal 32, 1065–1075.

Cobbold, P.R., 1999. Sand as an analogue material in tectonics; advantages, limitations and future developments. European Union of Geosciences Conference Abstracts 104 (1), 602.

Dahlen, F.A., 1984. Noncohesive critical coulomb wedges: an exact solution. Journal of Geophysical Research 89 (B12), 10125–10133.

Davis, D., Suppe, J., Dahlen, F.A., 1983. Mechanics of fold-and-thrust belts and accretionary wedges. Journal of Geophysical Research 88 (B2), 1153–1172.

Gutscher, M.A., Kukowski, N., Malavieille, J., Lallemand, S., 1996. Cyclical behavior of thrust wedges; insights from high basal friction sandbox experiments. Geology 24 (2), 135–138.

Han, C., Drescher, A., 1993. Shear bands in biaxial tests on dry coarse sand. Soils and Foundations 33 (1), 118–132.

Hoshino, K., Koide, H., Inami, K., Iwamura, S., Mitsui, S., 1972. Mechanical Properties of Tertiary Sedimentary Rocks Under High Confining Pressure, Kawasaki, 200pp.

Hubbert, M.K., 1937. Theory of scale models as applied to the study of geological structures. Geological Society of America Bulletin 48, 1459–1520.

Hubbert, M.K., 1951. Mechanical basis for certain familiar geologic structures. Geological Society of America Bulletin 62 (4), 355–372.

Huiqi, L., McClay, K.R., Powell, D., 1992. Physical models of thrust wedges. In: McClay, K.R., (Ed.), Thrust Tectonics, Chapman & Hall, London, pp. 71–81.

Jaeger, J.C., Cook, N.G.W., 1969. Fundamentals of Rock Mechanics, Methuen, London, 515pp.

Kopp, H., Klaeschen, D., Flueh, E.R., Bialas, J., 2002. Crustal structure of the Java margin from seismic wide-angle and multichannel reflection data. Journal of Geophysical Research 107 (B2), ETG 1-1–ETG 1-24.

Koyi, H., 1997. Analogue modelling; from a qualitative to a quantitative technique; a historical outline. Journal of Petroleum Geology 20 (2), 223–238.

Krantz, R.W., 1991. Measurement of friction coefficients and cohesion for faulting and fault reactivation in laboratory models using sand and sand mixtures. Tectonophysics 188, 203–207.

Lallemand, S.E., Lewis, K.B., Collot, J.Y., 1994. Sandbox modelling of seamount subduction and possible applications in New Zealand. In: Neil, H., Gillespie, J.L., Moon, V., Briggs, R. (Eds.), Geological Society of New Zealand 1994 Annual Conference. Geological Society of New Zealand, Christchurch. Geological Society of New Zealand Miscellaneous Publication 80a, p. 109.

Lallemand, S.E., Schnuerle, P., Malavieille, J., 1994b. Coulomb theory applied to accretionary and nonaccretionary wedges; possible causes for tectonic erosion and/ or frontal accretion. Journal of Geophysical Research 99 (6), 12,033–12,055.

Malavieille, J., 1984. Modélisation expérimentale des chevauchements imbriqués: application aux chaines de montagnes. Societé Géologique de France Bulletin 7, 129–138.

Marone, C., 1998. Laboratory-derived friction laws and their application to seismic faulting. Annual Review Earth & Planetary Science Letters 26, 643–696.

Moore, G.F., Taira, A., Klaus, A., Shipboard Scientific Party, 2001. Deformation and Fluid Flow Processes in the Nankai Trough Accretionary Prism. Proceedings of the Ocean Drilling Program, Initial Reports, 190.

Morgan, J.K., Karig, D.E., Maniatty, A., 1995. The estimation of diffuse strains in the toe of the western Nankai accretionary prism; a kinematic solution. Journal of Geophysical Research 99 (4), 7019–7032.

Mulugeta, G., 1988. Modelling the geometry of Coulomb thrust wedges. Journal of Structural Geology 10, 847–859.

Mulugeta, G., Koyi, H., 1992. Episodic accretion and strain partitioning in a model sand wedge. Tectonophysics 202 (2–4), 319–333.

Paterson, M.S., 1978. Experimental Rock Deformation, Springer, New York, 254pp.

Paterson, M.S., 2001. Relating experimental and geological rheology. In: Dresen, G., Handy, M. (Eds.), Deformation Mechanisms, Rheology and Microstructures 90, Springer International, Berlin, pp. 157–167.

Platt, J.P., 1986. Dynamic of orogenic wedges and the uplift of high-pressure metamorphic rocks. Geological Society of America Bulletin 97, 1037–1053.

Rutter, E.H., 1972. The effects of strain-rate changes on the strength and ductility of Solenhofen limestone at low temperatures and confining pressure. International Journal of Rock Mechanics and Mining Sciences 9, 183–189.

Schanz, T., Vermeer, P.A., 1996. Angles of friction and dilatancy of sand. Géotechnique 46 (1), 145–151.

Schellart, W.P., 2000. Shear test results for cohesion and friction coefficients for different granular materials; scaling implications for their usage in analogue modelling. Tectonophysics 324 (1–2), 1–16.

Scholz, C.H., Engelder, J.T., 1976. The role of asperity indentation and ploughing in rock friction. I. Asperity creep and stick-slip. International Journal of Rock Mechanics and Mining Sciences 13, 149–154.

Schulze, D., 1994. Entwicklung und Anwendung eines neuartigen Ringschergerätes. Aufbereitungstechnik 35 (10), 524–535.

Sibson, R.H., 1974. Frictional constraints on thrust, wrench and normal faults. Nature 249, 542–544.

Terzaghi, K., 1943. Theoretical Soil Mechanics, John Wiley, New York, 510 pp.

Vaid, Y.P., Sasitharan, S., 1992. The strength and dilatancy of sand. Canadian Geotechnical Journal 29, 522–526.

Wang, W.H., Davis, D.M., 1996. Sandbox model simulation of forearc evolution and noncritical wedges. Journal of Geophysical Research 101 (5), 11,329–11,339.

Willett, S.D., 1992. Dynamic and kinematic growth and change of a Coulomb wedge. In: McClay, K.R., (Ed.), Thrust Tectonics, Chapman & Hall, London, pp. 19–31.

Zhao, W.-L., Davis, D., Dahlen, F.A., Suppe, J., 1986. The origin of convex accretionary wedges; evidence from Barbados. Journal of Geophysical Research 91, 10246–10258.